CHARACTERIZATION OF AN E2V CHARGE-COUPLED DEVICE FOR THE MICHELSON INTERFEROMETER FOR GLOBAL HIGH-RESOLUTION THERMOSPHERIC IMAGING INSTRUMENT

by

James Beukers

A thesis submitted in partial fulfillment
of the requirements for the degree

of

MASTER OF SCIENCE

in

Electrical Engineering

Approved:

Dr. Todd Moon Major Professor	Dr. Jed Hancock Committee Member
Dr. Ryan Gerdes Committee Member	Dr. Mark R. McLellan Vice President for Research and Dean of the School of Graduate Studies

UTAH STATE UNIVERSITY
Logan, Utah

2015

Abstract

Characterization of an e2v Charge-Coupled Device for the Michelson Interferometer for Global High-resolution Thermospheric Imaging Instrument

by

James Beukers, Master of Science

Utah State University, 2015

Major Professor: Dr. Todd Moon
Department: Electrical and Computer Engineering

This thesis presents the characterization process of the camera system to be used in the Michelson Interferometer for Global High-resolution Thermospheric Imaging (MIGHTI) instrument on the National Aeronautics and Space Administration's (NASA) Ionospheric Connection Explorer (ICON) satellite. ICON will make measurements of the Ionosphere to understand the connection between terrestrial weather and the conditions of the ionosphere. MIGHTI will use Spatial Heterodyne Spectroscopy (SHS) to determine the Doppler shift of atomic oxygen airglow emission lines, from which ionospheric wind speeds are calculated.

The camera system for MIGHTI was built and characterized by the Space Dynamics Laboratory (SDL). At the heart of the camera is an e2v 4280, which is a 2k x 2k, back-illuminated, frame transfer Charge-Coupled Device (CCD). The camera system is designed for low read noise, low dark current, and a large dynamic range. An explanation of the data collection methods and analysis steps used to find the performance metrics of the system are presented. Also, the changes and optimization steps needed to meet performance requirements are described. Lastly, a summary of the results are given.

The system met all requirements, reaching a read noise of less than 6 electrons rms. The dark current was extremely low as well, less than 0.01 electrons per pixel per second

at -45°C. With this performance the instrument is able to collect high quality images used to accurately measure ionospheric wind speeds and directions.

(79 pages)

Public Abstract

Characterization of an e2v Charge-Coupled Device for the Michelson Interferometer for Global High-resolution Thermospheric Imaging Instrument

by

James Beukers, Master of Science

Utah State University, 2015

Major Professor: Dr. Todd Moon
Department: Electrical and Computer Engineering

This thesis presents the characterization process of an imaging device for a satellite. The camera system was built by the Space Dynamics Laboratory (SDL) and will be used in the Michelson Interferometer for Global High-resolution Thermospheric Imaging (MIGHTI) instrument for National Aeronautics and Space Administration's (NASA) Ionospheric Connection Explorer (ICON) satellite. This mission will further scientists' understanding of the connection between the Earth's weather and ionospheric conditions. The ionosphere, a part of the atmosphere, interferes with satellite communications causing disturbances and disruptions. By learning more about the ionosphere through the data collected by this instrument, scientists will better understand its effects on our communications.

Acknowledgments

I would like to thank the Space Dynamics Laboratory (SDL) for the facilities and the opportunity to take on this thesis project. I would like to thank Jed Hancock for encouraging me to do a thesis and making it possible. Many at SDL provided mentoring and help over the course of this thesis including James Cook and Mitch Whiteley. This project would not be possible without the funding for the Ionospheric Connection Explorer (ICON) mission from the Naval Research Laboratory (NRL) and the National Aeronautics and Space Administration (NASA). I would also like to thank professors Dr. Todd Moon, and Dr. Ryan Gerdes from Utah State University (USU) for participating on my thesis committee and giving feedback and advice throughout the thesis writing process. I must also thank Dr. Charles Swenson, from USU, for being available to participate in my thesis defense. Lastly I would like to thank my wife Jen and my daughter Rachel for their support.

James Beukers

Contents

List of Tables

List of Figures

Chapter 1

Introduction

This chapter presents an introduction of the Michelson Interferometer for Global High-resolution Thermospheric Imaging (MIGHTI) instrument on the National Aeronautics and Space Administration's (NASA) Ionospheric Connection Explorer (ICON) mission. This mission will further scientists' understanding of the connection between the ionosphere and terrestrial weather. The ionosphere, a part of the Earth's atmosphere, has many nonlinear behaviors which interfere with satellite communications causing disturbances and disruptions [2]. Scientists will better understand the connection between the ionosphere and terrestrial weather as well as its effects on our communications from the data collected by the ICON mission.

1.1 MIGHTI Instrument

The MIGHTI instrument (see Fig. 1.1, [2]) will be used to measure thermospheric winds and temperatures. Wind measurements will be made between 90-300km altitude and are calculated from the Doppler shift of atomic oxygen airglow emission lines (630nm and 557.7nm). The temperature is calculated from the shape of the O2 A-band emission (762nm) (see Fig. 1.2) [3]. There will be two sensor units with orthogonal fields of view, 45° and 135° from the spacecraft's motion, allowing two perpendicular measurements of the same location less than eight minutes apart [3]. Having these two perpendicular measurements provides an altitude profile of wind vectors.

A Michelson interferometer will be used to collect an interferogram from which the Doppler shift is found. To simplify the design and on-orbit operations, MIGHTI will be using a Spatial Heterodyne Spectroscopy (SHS) approach which will replace movable mirrors with fixed, tilted diffraction gratings. The design of the MIGHTI interferometer is shown

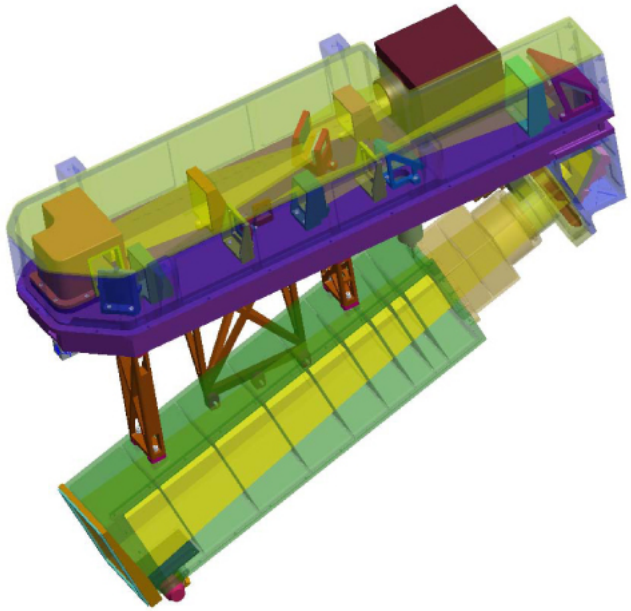

Fig. 1.1: Conceptual design of NRL's MIGHTI instrument.

Fig. 1.2: NASA false color image of oxygen emission lines at night.

in Fig. 1.3 [3].

After going through the interferometer, the light continues through an optical setup that separates the green and red light to different sides of the detector. Before reaching the detector, which is a Charge-Coupled Device (CCD) further described in section 1.2, the light is filtered by a narrow-band mosaic filter. This filter helps to collect only the wavelengths of interest, Fig. 1.4 shows a model of the filter and the desired wavelengths [4].

After passing through the filter, the interferogram is captured by the CCD and the desired information is then extracted from the data collected. In order for the MIGHTI instrument to work properly the image collected by the CCD must have enough contrast and resolution to extract the interferogram. This leads to special requirements which will be discussed in Chapter 2.

1.2 MIGHTI CCD Camera System

Each CCD is contained inside a camera head shown in Fig. 1.5 [5]. Both camera heads are connected to the camera electronics box which is shown in Fig. 1.6 [5]. Within the camera head, the CCD is attached to the camera preamp as shown in Fig. 1.7 [6]. The preamp interfaces the CCD with the bias voltages and clock signals from the camera electronics box. It also takes the CCD output and converts it into a differential signal before transmitting it through the cables to the camera electronics box. This is to reduce noise that is picked up during transmission through the cables. Also shown in Fig. 1.7, the camera heads properly align the CCD to the instrument and contain thermal links and a thermoelectric cooler (TEC) to maintain the CCD at the desired operating temperature. The camera heads and camera electronics box were designed and built at the Space Dynamics Laboratory (SDL). The camera electronics box contains several different boards with varying functions. The Power Supply Board (PSB) contains the necessary elements to convert the power received from the satellite into the proper voltages for the CCD and electronics operations. The Digital Board (DB) contains the clocks and digital signal processing required to operate the instrument. The Analog Board (AB) contains the low noise analog chains that take the signal from the CCD and convert it into digital numbers (DN). Chapters 3 and 4 give the

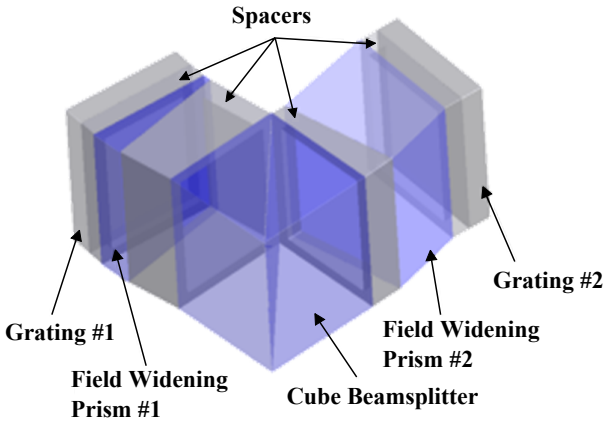

Fig. 1.3: Design for the MIGHTI interferometer.

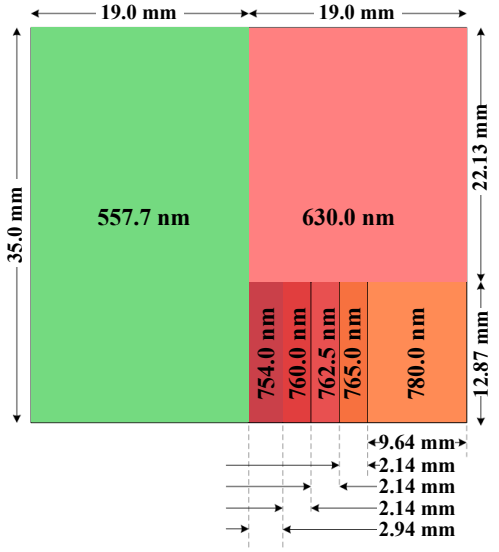

Fig. 1.4: Mosaic filter.

test plans and procedures that were used to verify proper functionality of the devices.

A CCD is an electronic device used to convert incident light into electrical signals. To do this it uses the photoelectric effect; when a photon strikes the silicon its energy is transferred to an electron and gives rise to an electron-hole pair. Due to an electric potential created by an array of electrodes on the surface of the device, the electron and the hole are separated. The photo-generated electron is then captured in a potential well, known as a pixel [7]. As this occurs, more and more charge collects in each pixel, corresponding to the number of photons that hit it. An image can then be pieced together by reading out the charge in each pixel as it is shifted out of the device. While CCDs have improved greatly since their invention, there are inefficiencies in this process that require the system to be characterized to quantify the uncertainties.

The uncertainties of the camera system come from the process of converting photons to DN as the CCD records the image. Camera system characterization quantifies the uncertainties, or noise, associated with the process of image capture. The quality of the image can be improved by removing certain amounts of noise and bias levels discovered through the characterization process. One removable type of noise is fixed pattern noise (FPN). As the name states, this noise is fixed, or consistent from image to image and can be removed from the collected image once it has been characterized. FPN is due to multiple causes, including different responsivity of each pixel in the array, differences in clock drive

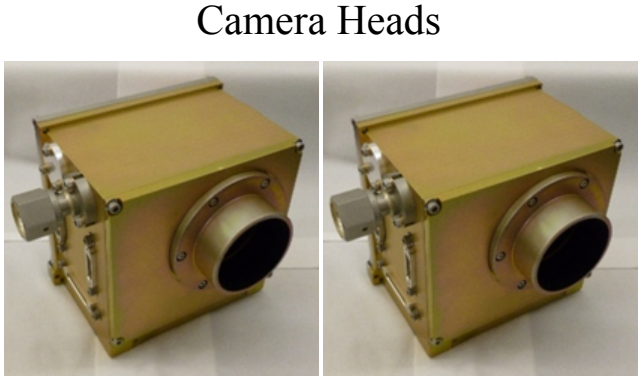

Fig. 1.5: Camera heads.

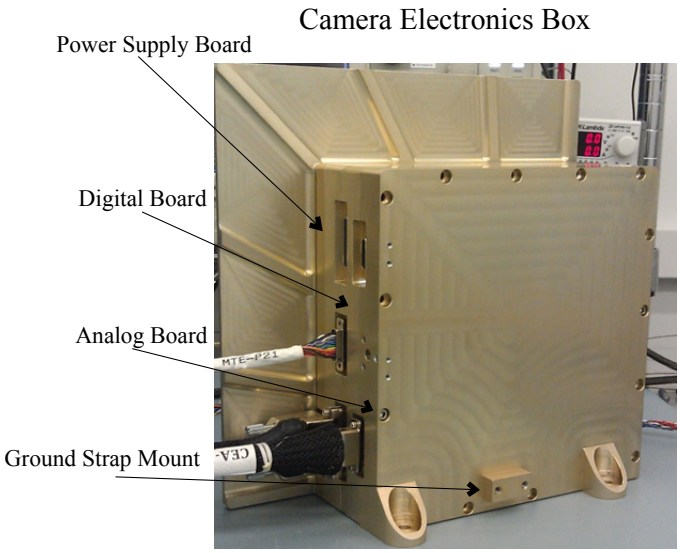

Fig. 1.6: Camera electronics box.

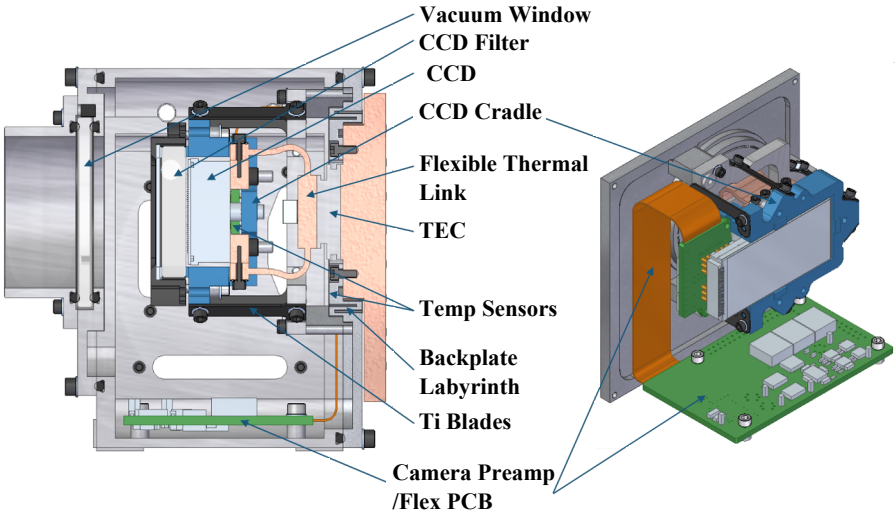

Fig. 1.7: Camera preamp contained inside of the camera head.

voltages, and dust particles on the detector.

Another imperfection in the image quality comes from dark current. Dark current is the rate at which thermally generated electrons are captured in the pixels. There is no way to differentiate these electrons from those captured by photon interaction and thus more noise, called dark noise, is added. Dark noise occurs in all CCDs and is highly dependent on the substrate design and temperature of the device.

Read noise is another noise characteristic defined as the number of electrons that are added to the signal from the CCD electronics during charge readout. Read noise sets the base level for the characteristic called dynamic range which is "the ratio of the maximum detectable light intensity to the minimum detectable light intensity" [7]. The maximum level is set by the saturation limit of the device, or how many electrons each potential well can hold before it begins to overflow. This is also called the full well capacity (FWC).

Another important performance characteristic is the gain nonlinearity. It is the measurement of how linearly the output signal in DN relates to the number of electrons in a potential well for the dynamic range of the device.

Table 1.1 gives a summary of each performance metric. These parameters will be described in greater detail as the characterization plan and procedures are laid out. Characterization was necessary not only to verify that the camera system met requirements but also to help optimize the camera system before integration to the MIGHTI instrument.

Table 1.1: Performance characterization metrics [1].

Performance Metric	**Description**
Read Noise	Any noise that is not a function of signal. This is the noise added by the device electronics during charge readout
Dark Current	The rate of generation of thermally generated electron accumulation
Dark Offset	The camera's output DN level in total absence of signal electrons
Gain	The number of electrons that determine each DN step distinguished by the readout electronics
Gain Nonlinearity	The residual nonlinearity in the gains across the dynamic range of the device
FWC	The maximum number of electrons that each pixel well on average can contain
Dynamic Range	The ratio of pixel full well to read noise
VCTE	Vertical Charge Transfer Efficiency: measurement of how efficiently each pixel charge is transferred from one row to the next
HCTE	Horizontal Charge Transfer Efficiency: measurement of how efficiently each pixel charge is transferred from one column to the next
FPN	Fixed Pattern Noise: Noise introduced because of the varying sensitivities of each pixel. Not each pixel is created exactly the same because of imperfections in the silicon and in the manufacturing process

Chapter 2

MIGHTI CCD Camera Requirements

Camera requirements were given to ensure that the instrument system would perform properly and collect interferograms that will result in science data meeting mission requirements to measure thermospheric winds as a function of altitude. The camera requirements are listed in Appendix A and a description of why each one is necessary is given here.

2.1 Physical Requirements

Physical requirements were given to outline the size and operation of the camera system (see Appendix A.1). Requirement one is that the device must be a frame transfer device, or operate with an electronic shutter. There are two main CCD architectures with electronic shutters known as interline transfer and frame transfer. With interline transfer devices, every other column is a storage area insensitive to light (see Fig. 2.1). This allows each column of the image to quickly be shifted into the storage area adjacent to it, later to be read out row by row while another image is being taken. Frame transfer devices also have a storage area but it is below the image area (see Fig. 2.1).

In a frame transfer device, once the image has been captured, the whole image frame is transferred quickly down into the storage area row by row, leaving the image area empty to collect another image. The frame transfer architecture was chosen because each column in the image area is light sensitive unlike the interline transfer architecture that contains the storage areas.

Requirement two is that the device must have binning capability. This allows pixels to be combined on the CCD into 'super pixels' before being read out. This reduces the image resolution and size but increases the amount of signal per pixel, which increases the signal to noise ratio (S/N). Binning also reduces the required time to read out the entire image

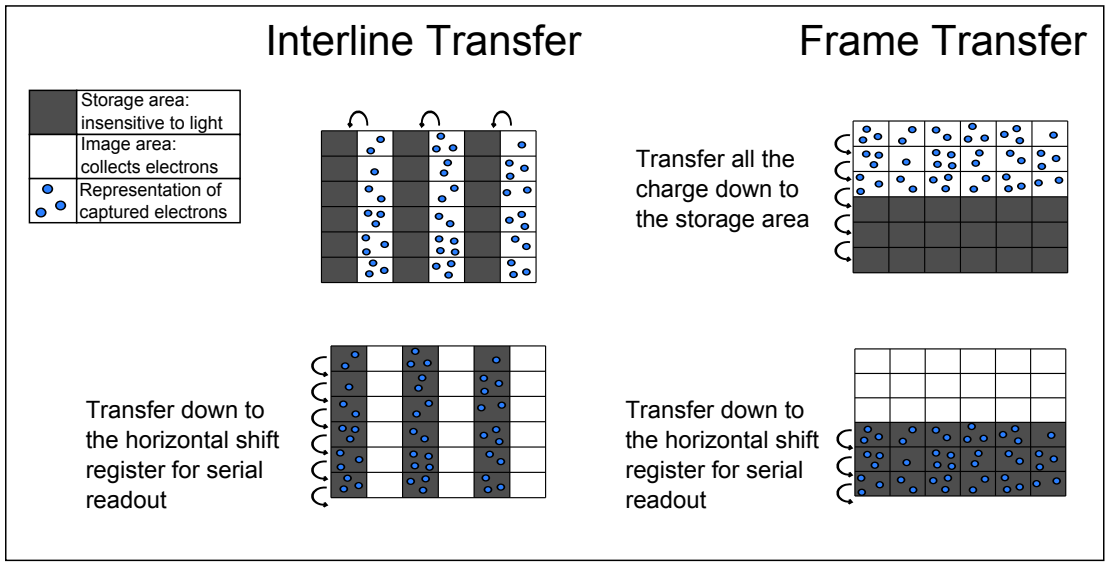

Fig. 2.1: Example of different CCD architectures.

because there are less pixels to digitize. A 2x16 binning mode will be used for flight, where 2 rows and 16 columns will be binned together into a super pixel.

Requirement three is a goal of quantum efficiency (QE). QE is a measurement of the ability of a semiconductor to produce electron-hole pairs from incident photons [8]. A high QE gives a higher system throughput and is the best way to increase the signal-to-noise ratio.

Requirements four and five were set to ensure that the temperature of the CCD could be controlled. Cooled to $-45°C$ to significantly reduce dark current, and heated to drive off any water that may accumulate on the CCD during orbit.

Requirements six and seven are to ensure that there is no stray light and that all of the desired signal is let through the optical components to the CCD.

Requirement eight defines the versatile operation required by the camera system. The system can be operated at atmosphere and in space.

2.2 Camera Readout Requirements

Camera readout requirements were given to ensure that the supporting camera electronics will not limit the performance of the CCD camera system. In order for accurate wind and temperature measurements to be made, the image collected by the CCD must have enough contrast and resolution to detect the interferogram. An example interferogram is shown in Fig. 2.2 [4].

Due to the close spacing of the interference fringes and the low contrast and intensity at high altitudes, it is important that the read noise and dark current be low to properly detect the interference pattern. Scientists calculated that a read noise of $\leq 10e^-$ rms and a dark current rate of $\leq 0.13e^-$/pixel/sec is necessary (see A.2 1 and 3).

By differing the exposure time, or the amount of time that the CCD is exposed to the image, the signal level of the image can be shifted. Requirement two is set so that a large range of exposure times is available if adjustments are needed depending on the differing intensities of the scene both night and day.

Requirement four sets the frame transfer time. Once the exposure time is finished, the image is transfered into the storage area on the CCD. As the transfer happens, each row is shifted across the image area. This means that each row is exposed to the same image that the previous row was exposed too. If this transfer does not happen fast enough the image can become blurred; however, it takes time for electrons to move, so transfer times must not be too fast or the charge is not efficiently transferred from one row to the next.

As the image is waiting in the storage area of the CCD for readout, it is still collecting dark current. The longer it takes to readout, the more dark current is collected. Requirement five was set to minimize the amount of dark current collected during readout time yet allow time for each pixel to be accurately digitized.

Requirement six, in conjunction with the low read noise, is to ensure that the conversion from analog signals to digital numbers maintains a very high resolution.

As mentioned above, the interferogram has dark and bright fringes, also at higher altitudes the contrast is lower, and near the earth, at lower elevations, the image will be

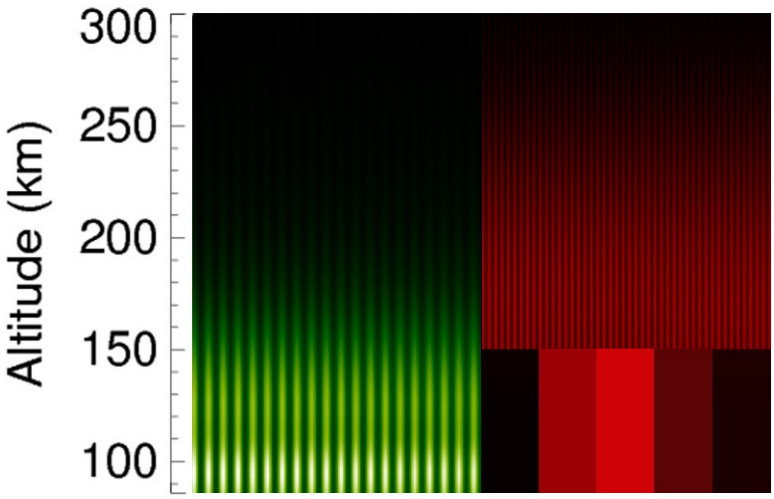

Fig. 2.2: An example of the interferogram that will be measured.

much brighter. In order to measure both the bright and dim interference patterns the device must have a large enough dynamic range. A large factor in dynamic range is the FWC, which was calculated to be $\geq 100,000$ electrons (see A.2 7). Requirement eight sets the linearity of the device over its dynamic range, this is important because the accuracy of the measurements at both high and low signals is dependent on the linearity.

Many of these requirements were met by SDL in the physical design and selection of the camera system components. Table 2.1 lists the performance requirements that required characterization to verify.

Table 2.1: Driving requirements for characterization.

Parameter	**Value**
Read Noise	≤ 10 electrons rms
Dark Current	$\leq$ 0.13 electrons/s at -45°C for a 13.5 μm square pixel.
Residual nonlinearity	$\leq 1\%$ rms across the dynamic range after nonlinearity correction.

Chapter 3

Test Plan

This chapter presents the characterization plan for the MIGHTI camera system on NASA's ICON mission. Details of the CCD used in the camera system can be found on the manufacturer's data sheet included in Appendix B. The characterization plan will describe the processes that were used to find the performance characteristics of the device as listed in Table 1.1. The goal of this testing was to characterize the engineering model CCD performance to help in the adjustments of the electronics as well as to verify that system requirements were met.

3.1 Characterization Plan

The data collections were carried out at SDL using the test hardware and software created by SDL. The data was collected in a temperature- and light-controlled chamber to allow characterization of the device at multiple temperatures and light intensities. The performance parameters were calculated using several different tests: dark response, Photon Transfer Curve (PTC), Vertical and Horizontal Charge Transfer Efficiency (VCTE, HCTE) using the Extended Pixel Edge Response (EPER) method. The data collected from these tests was then reduced into the performance metrics as explained in Chapter 5 using a series of Matlab scripts. Other tests were also performed to find other parameters such as crosstalk between the two output taps of each CCD and between the two camera heads.

3.1.1 Characterization Tests

3.1.1.1 Dark Response

The performance metrics obtained through the dark response test include dark current ($[e^-/pixel/sec]$), dark offset ($[e^-][DN]$), and read noise ($[e^-][DN]$). To collect dark

response data it is necessary to shut out all light sources and provide a dark background for the detector array. In testing it was found that dark current at $-45°C$ is very low and could not easily be measured with the test setup used. By taking measurements at $0°C$, the dark current is several orders of magnitude higher, and more easily measured with short integration times. Integration time is the amount of time that charge is collected in each pixel before frame transfer occurs. Thus data for dark current was taken at $0°C$ in the unbinned operating mode at four different integration times. Data to determine dark offset and read noise is taken at $-45°C$ in both the unbinned and binned mode for a single integration time.

3.1.1.2 Photon Transfer Curve (PTC)

The performance metrics obtained through the PTC include gain ($K[e-/DN]$), gain nonlinearity ($NL[\%]$), full well capacity (FWC $[e^-/pixel]$), and dynamic range ($DR[DN]$). The photon transfer curve is a measurement of mean response and noise observed over a range of signal levels. The data is collected at many data points throughout the dynamic range, from the smallest light exposure to saturation. A Light Emitting Diode (LED) is used as the light source and different length pulses are used to set the exposure, while the integration time of the CCD remains constant. Through testing it was found that 50 data points were sufficient to create a well defined PTC. In order to characterize the CCD in both the unbinned and 2x16 binned operating modes, PTC data is collected for each mode at $-45°C$.

3.1.1.3 Vertical Charge Transfer Efficiency (VCTE)

This test measures the VCTE of the CCD. VCTE will be calculated from the EPER method. The EPER method is done using an LED to uniformly expose the CCD to light and clocking out more rows into the readout register than are actually present (see Fig. 3.1). These are called overscan rows and do not represent physical pixels, but are values created by the readout electronics. This method measures CTE by counting the charge that is trapped during transfer. To do this we measure how much charge was left behind in the

overscanned pixels. This method is slightly optimistic due to the fact that small amounts of charge left per pixel are hard to distinguish from the noise [9].

3.1.1.4 Horizontal Charge Transfer Efficiency (HCTE)

This test measures the HCTE of the CCD. HCTE will be calculated from the EPER method as well, but more columns instead of rows are clocked into the readout register than are actually present. These are called overscan columns similar to the overscan rows described in Section 3.1.1.3 (see Fig. 3.1).

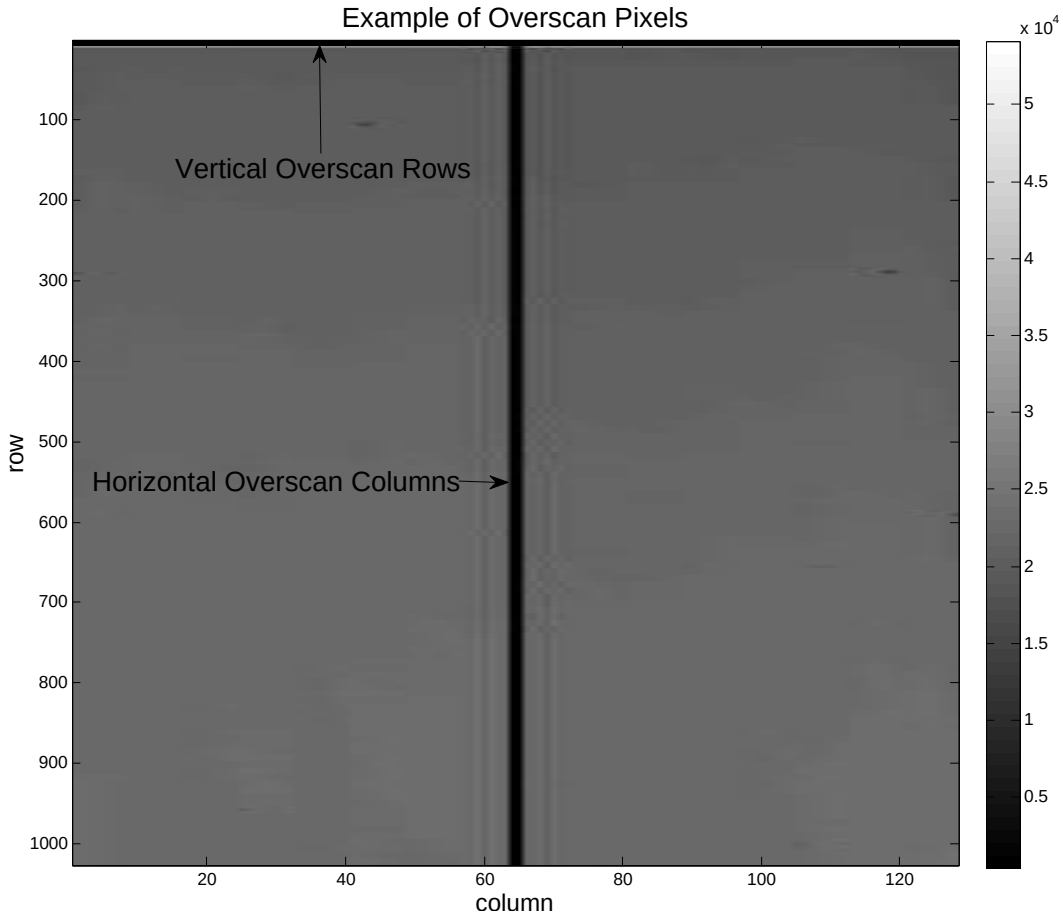

Fig. 3.1: Dark image showing where vertical and horizontal overscan pixels are created.

Chapter 4

Data Collection Procedures

This chapter describes the procedures for collecting the necessary data to characterize the CCD camera.

4.1 CCD PERFORMANCE

The following tests represent a typical data collection suite for CCD characterization. Data will be collected using the MIGHTI Test Software and will be done one camera at a time.

4.1.1 Dark Response Data Collection

To collect the dark response data it is necessary that the CCD is in complete darkness so that the only charges collected are due to dark current. It is also necessary that the CCD be at $-45°C$ to verify requirements at this operating temperature. To improve the accuracy of the dark offset measurements, ten images will be taken. Images will be collected at an integration time of 2500 ms for binned and 4000 ms for unbinned operation. These integration times match the integration times used in the corresponding PTC data collections.

As was explained in Chapter 3, dark response data will also be collected at $0°C$ to calculate dark current. Ten images will be taken at integrations of 20, 40, and 60 seconds in the unbinned mode.

4.1.2 Charge Transfer Efficiency (HCTE and VCTE)

CTE data will only be collected in the unbinned mode. To reduce the time required to collect the necessary data, both the HCTE and VCTE data will be combined in the same data collections. This is done by enabling 16 horizontal overscan columns and 16 vertical

overscan rows in each image. The data will be collected near 50% full well. To achieve this, the LED intensity is slowly increased until an output signal level of 30k DN is reached.

4.1.3 Photon Transfer Curve (PTC)

PTC data may be collected both in the 2x16 binned and unbinned mode to assist in camera characterization, however, the requirements to be met are specified for the 2x16 binned mode operation. PTC data may be collected at different temperatures to better understand the system over a temperature range, however, for the requirements to be met, data was collected at $-45°C$.

Before collecting PTC data, it is necessary to determine the pixel saturation point. In order to be consistent with data, it was chosen to maintain the same LED pulse width files for each test but to adjust the LED voltage supply up or down to find the saturation point. The pulse widths ranged from 1ms to 250ms for the 2x16 binned mode and from 16ms to 3.6s for the unbinned mode. In order to find the saturation point the LED pulse width is set to the maximum pulse width value (250ms for 2x16 binned and 3.6s for unbinned). Then the LED voltage supply is adjusted up or down between image captures until the pixel saturation point is found.

To create the PTC the CCD is incremented from complete darkness to full well. This can either be done by increasing the exposure time, allowing more time for photons to interact with each pixel, or by increasing the light intensity, which creates more photons to interact with each pixel. At each incremented level, two images are captured which will then be subtracted from each other to eliminate FPN. Before plotting the average signal, the Analog to Digital Converter (ADC) offset must be removed from the raw data. This offset level represents the signal measured when no electrons were generated from interacting photons. This was found using the dark images as previously described, however, it can also be measured from overscanned pixels. Virtual overscanned pixels are created by the readout electronics when more pixels are clocked out than actually exist. The average of these pixels is a good representation of the offset level [8, p. 50-51]. The noise is then calculated and plotted against the average signal to create the curve. An example curve is

shown in Fig. 4.1.

The PTC contains four regions:

1. Read Noise, with a slope of zero, where the graph is dominated by the read noise.
2. Shot Noise, where the Noise is proportional to the square root of the signal intensity thus giving a slope of 1/2 on the log-log plot.
3. FPN, where the fixed pattern noise is equal to the signal intensity thus creating a slope of 1.
4. Full Well, when the pixels begin to saturate thus suppressing random noise [1, p. 102].

By taking two identical images and subtracting them the FPN can be removed, thus extending the shot noise slope of 1/2 until full well occurs (see Fig. 4.2).

4.2 Conclusion

In certain circumstances data was needed faster and data collections were a very lengthy process, especially if cold temperature tests were needed. To reduce the time it took to collect data, the HCTE and VCTE tests were included in the PTC test by enabling overscan in the PTC images. This reduced the accuracy of the results due to only having two images to average instead of ten; however, the data was sufficient for use and sped up the process by twenty minutes or more in the unbinned mode. After data collection, the data is reduced

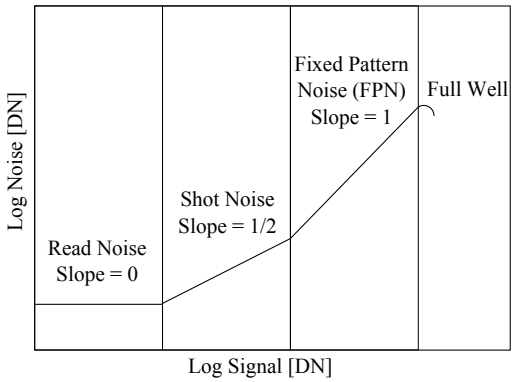

Fig. 4.1: Description of PTC.

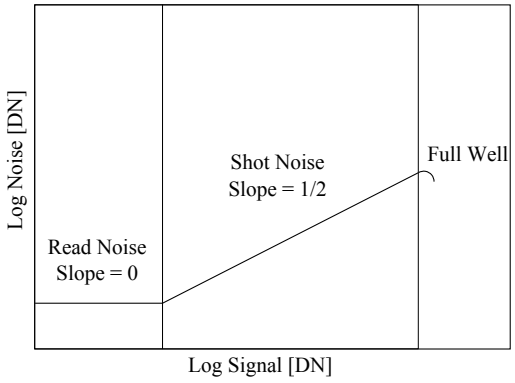

Fig. 4.2: PTC with FPN removed.

into the performance characteristics as explained in Chapter 5 using a series of Matlab scripts. These characteristics are then compared to the requirements (see Chapter 2) to verify proper functionality.

Chapter 5

Data Analysis

This chapter will describe how the data collected is analyzed and reduced into performance metrics.

5.1 Read Noise

From the dark response data, read noise can be calculated first by taking the standard deviation of each pixel for the ten images taken over a region of interest:

$$\sigma = \sqrt{\frac{1}{N}\sum_{i=1}^{N}(p_i - \mu)^2}. \tag{5.1}$$

Where $\mu = \frac{1}{N}\sum_{i=1}^{N} p_i$, p_i is the signal level of the same pixel for each image i out of the total $N = 10$ images taken. The region of interest was chosen as shown in Fig. 5.1.

This creates a standard deviation profile as seen in Fig. 5.2 which is then averaged to get the mean read noise:

$$\sigma_R[DN] = \frac{1}{N_p}\sum_{i=1}^{N_p}\sigma_i, \tag{5.2}$$

where N_p is the total number of pixels in the region chosen.

5.2 Dark Current

Dark current is also calculated from the dark response images. First, the average dark signal level (DarkS) over the chosen region is calculated for each exposure time $t[s]$:

$$DarkS_t[DN] = \frac{1}{N_p}\sum_{i=1}^{N_p} p_i. \tag{5.3}$$

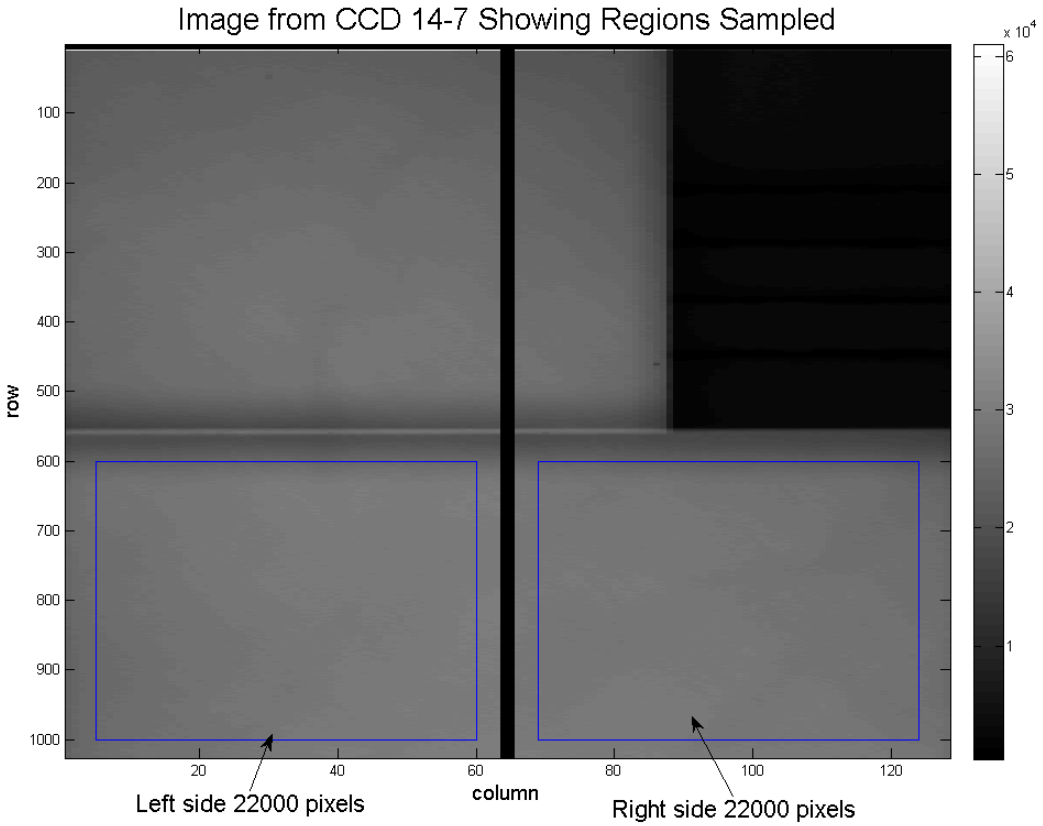

Fig. 5.1: Image showing regions and number of pixels sampled.

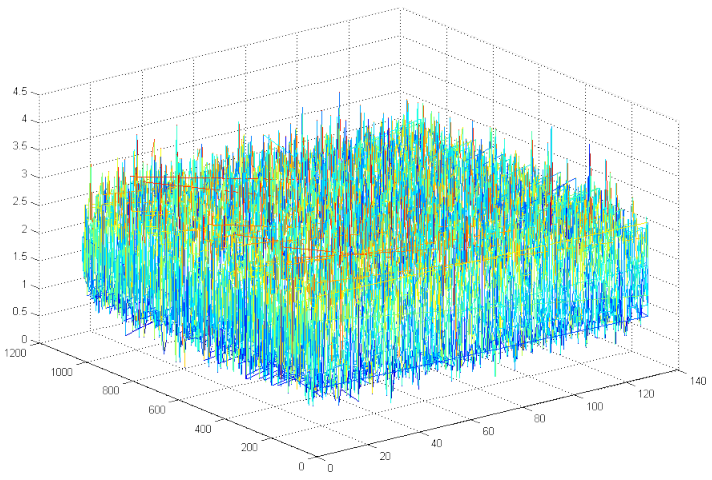

Fig. 5.2: Standard deviation profile.

These values are then plotted versus the exposure time. The dark current rate (DC) in units of $DN/pixel/sec$ is then calculated as the slope of the best fit line to these N_t points:

$$DC = \frac{N_t \sum t * DarkS - \sum t \sum DarkS}{N_t \sum (t^2) - (\sum t)^2}. \tag{5.4}$$

It is then multiplied by the gain $K[e^-/DN]$, as explained in Section 5.3, to convert it to $e^-/pixel/sec$. An example plot is shown in Fig. 5.3.

This test can be completed at different temperatures to obtain dark current as a function of temperature. Because dark current at $-45°C$ is very low, it could not accurately be measured with the test setup used. Thus dark current was measured at $0°C$ and then using Eq. (5.5) provided by e2v, the rate was projected to $-45°C$. This equation can be used to project a dark current rate measured at any temperature T_1, to another temperature T_2. Eq. (5.5) was used to project the dark current in Fig. 5.3 to $-45°C$ as shown in Fig. 5.4.

$$Q_{T_2} = Q_{T_1} * \left(\frac{T_2}{T_1}\right)^3 * \frac{e^{-9080/T_2}}{e^{-9080/T_1}}. \tag{5.5}$$

5.3 Gain

To convert signal and noise measurements from DN into electrons, data is collected as described in Chapter 4. This data will then be used to calculate the system gain ($K[e-/DN]$) which is the number of electrons per DN. Gain nonlinearity ($NL[\%]$), full well capacity (FWC $[e^-/pixel]$), and dynamic range $DR[DN]$) are also derived from the data.

As shown in Fig. 5.5, a typical CCD camera can be represented by several transfer functions. The first three are related to the CCD while the last two are characteristic of the signal processing circuitry [1, p. 99]. The first two deal with the QE, the third is the CCD output amplifier sensitivity. The last two are the signal chain gain and the ADC gain, resulting in DN as output.

Instead of measuring each individual transfer function, which is difficult to do, they can all be collapsed into a single transfer function as depicted in Fig. 5.6 [8, p. 36]. Here the camera system can be thought of as a black box with interacting photons P as input,

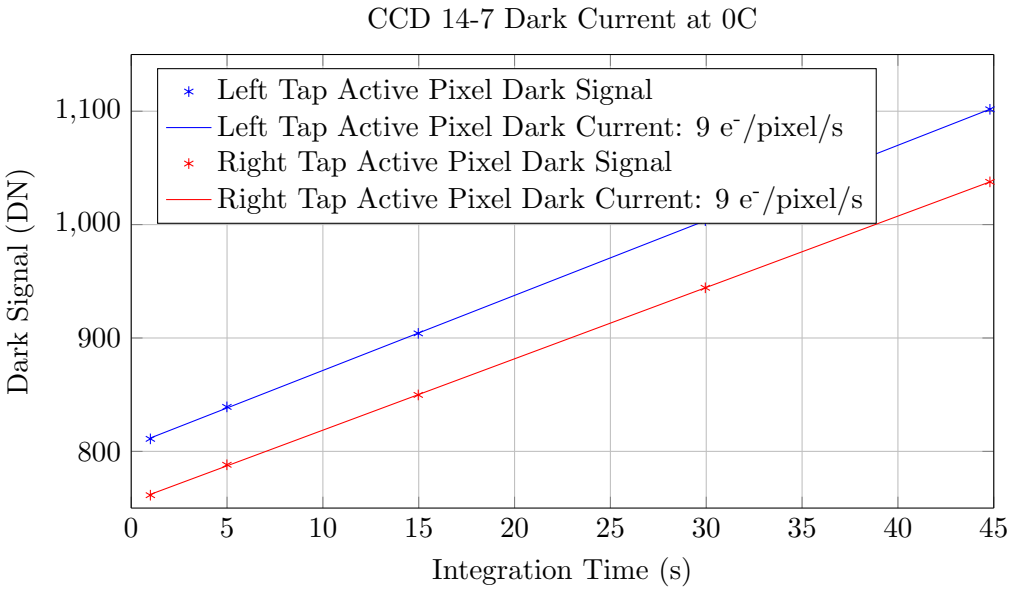

Fig. 5.3: Dark current calculation at $0°C$.

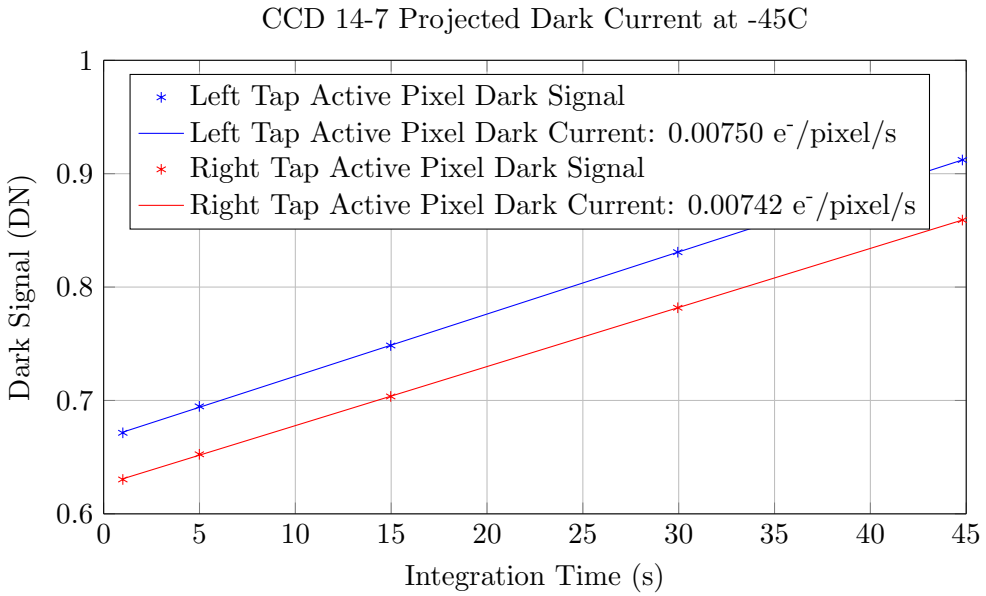

Fig. 5.4: Dark current projected from $0°C$ to $-45°C$.

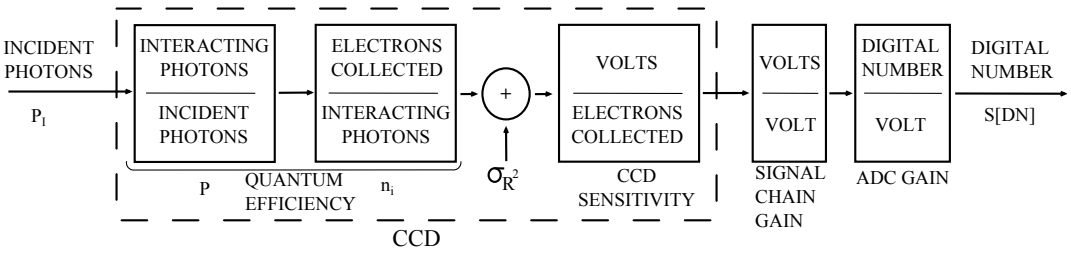

Fig. 5.5: CCD camera transfer functions.

a transfer function 1/K, and a measured signal $S[DN]$ as output. Due to the nature of photons, there is a known relationship between the input signal and the input noise called shot noise. The input signal is the mean signal level, or average number of interacting photons, and shot noise is related to the input by Eq. (5.6).

$$\sigma_P = \sqrt{P}. \tag{5.6}$$

From Fig. 5.6 the output can be related to the input as follows [8, p. 37]:

$$P = SK, \tag{5.7}$$

$$\sigma_P = \sigma_S K. \tag{5.8}$$

Now inserting these two equations into Eq. (5.6) we get,

$$\sigma_S K = \sqrt{SK}. \tag{5.9}$$

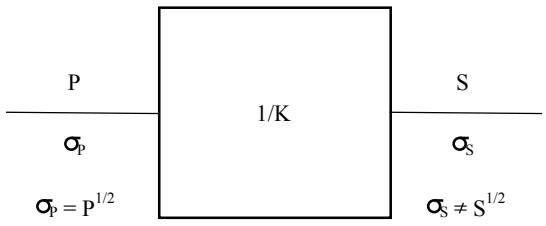

Fig. 5.6: Black box camera system.

Squaring both sides and solving for K,

$$K = \frac{S}{\sigma_S^2}. \tag{5.10}$$

From this result we see how we can calculate K from the relationship of the output signal to the output variance. Going further into detail in the derivation, the output signal can be related to the input photons as follows [1, p. 100]:

$$S[DN] = \frac{P}{K}, \tag{5.11}$$

where the constant K is the gain $[e^-/DN]$. This constant K can now be found by relating the output signal to its variance $\sigma_S^2[DN]$. The variance is found using the propagation of errors formula. First the partial derivative is taken with respect to each variable.

$$\delta S = \frac{\delta S}{\delta P}\delta P + \frac{\delta S}{\delta K}\delta K, \tag{5.12}$$

where $S = S[DN]$ for simplicity. Now squaring both sides and summing from $i = 1$ to N:

$$\sum_1^N (\delta S_i)^2 = \left(\frac{\delta S}{\delta P}\right)^2 \sum_1^N (\delta P_i)^2 + 2\left(\frac{\delta S}{\delta P}\right)\left(\frac{\delta S}{\delta K}\right)\sum_1^N (\delta P \delta K) + \left(\frac{\delta S}{\delta K}\right)^2 \sum_1^N (\delta K_i)^2. \tag{5.13}$$

Because P and K are uncorrelated, about half of the $\delta P \delta K$ terms are negative and half are positive, as it is a deviation around the mean. Thus the cross term will become zero in the summation as N becomes large. Canceling the cross terms and dividing both sides by $N - 1$,

$$\frac{\sum_1^N (\delta S)^2}{N-1} = \frac{(\frac{\delta S}{\delta P})^2 \sum_1^N (\delta P)^2}{N-1} + \frac{(\frac{\delta S}{\delta K})^2 \sum_1^N (\delta K)^2}{N-1}. \tag{5.14}$$

Now the standard deviation equation of S can be written as the variance (σ_S^2) of S as follows:

$$\frac{\sum_1^N (\delta S_i)^2}{N-1} = \frac{\sum_1^N (S_i - \bar{S})^2}{N-1} = \sigma_S^2. \tag{5.15}$$

Plugging this result into Eq. (5.14) gives us the final propagation of errors formula:

$$\sigma_S^2 = \left[\frac{\delta S}{\delta P}\right]^2 (\sigma_P^2) + \left[\frac{\delta S}{\delta K}\right]^2 (\sigma_K^2) + \sigma_R^2, \tag{5.16}$$

where the read noise floor variance σ_R^2 was added in quadrature as shown in Fig. 5.5. Read noise is not included earlier in the propagation of errors formula because it is independent of the number of photons and the gain. Carrying out the differentiations and assuming that $\sigma_K^2 = 0$ (how this is a reasonable assumption will be shown later in this chapter), the variance in S is found as follows:

$$\sigma_S^2 = \left(\frac{\sigma_P}{K}\right)^2 + \sigma_R^2, \tag{5.17}$$

$$K^2 = \left(\frac{\sigma_P^2}{\sigma_S^2 - \sigma_R^2}\right). \tag{5.18}$$

From photon statistics, $\sigma_P^2 = P$ and Eq. (5.11),

$$K^2 = \frac{SK}{\sigma_S^2 - \sigma_R^2}, \tag{5.19}$$

$$K = \frac{S}{\sigma_S^2 - \sigma_R^2}. \tag{5.20}$$

An example histogram of the gain values calculated according to Eq. (5.20) can be seen in Fig. 5.7 where the mean gain is taken to convert the DN counts into electrons to find the final performance metrics.

The variance of K can be found to quantify the accuracy of the calculated gain value [1, p. 111]. This is done by applying the propagation of errors formula to Eq. (5.20) rewritten as

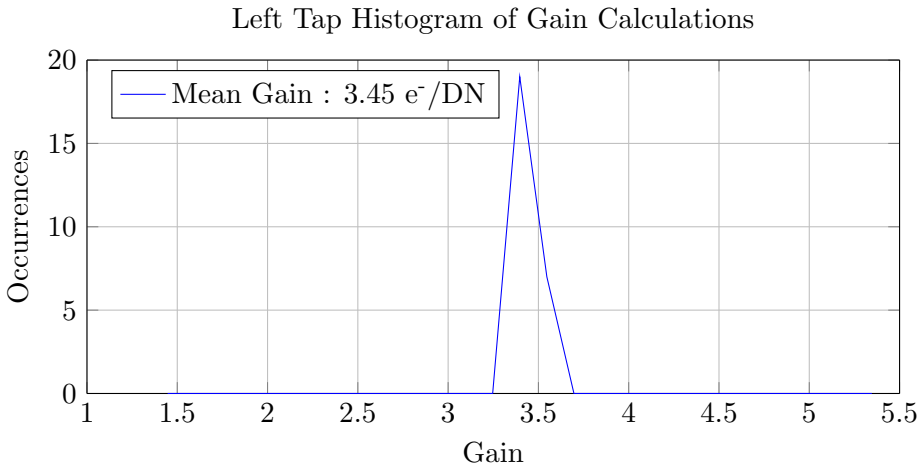

Fig. 5.7: Histogram of calculated gains.

$$K = \frac{S}{N^2}, \tag{5.21}$$

where the read noise, σ_R, is assumed negligible and $N = \sigma_S$. Now applying the propagation of errors formula in a similar manner as before yields

$$\sigma_K^2 = \left[\frac{\delta K}{\delta S}\right]^2 (\sigma_S^2) + \left[\frac{\delta K}{\delta N}\right]^2 (\sigma_N^2). \tag{5.22}$$

Using photon statistics, the uncertainty in both the signal and the noise measured are

$$\sigma_S^2 = \frac{S}{K N_{pix}}, \sigma_N^2 = \frac{N^2}{2N_{pix}}, \tag{5.23}$$

where N_{pix} is the number of pixels sampled. Substituting in these two equations and performing the differentiation required in Eq. (5.22) yields

$$\sigma_K^2 = \frac{1}{N^4}\frac{S}{K N_{pix}} + \frac{4S^2}{N^6}\frac{N^2}{2N_{pix}}. \tag{5.24}$$

Now using Eq. (5.21), this simplifies to

$$\sigma_K^2 = \frac{1}{N_{pix}}\left[K\left(\frac{1}{S} + 2K\right)\right]. \tag{5.25}$$

As long as $\sigma_S << S$, which is true for normal signal levels, this equation can be simplified further using the approximation $1/S << 2K$, giving the final result,

$$\sigma_K^2 = \frac{2K^2}{N_{pix}}. \tag{5.26}$$

This results shows that σ_K^2 can be reduced as much as desired by sampling more pixels. So as long as many pixels are sampled, the assumption that $\sigma_K^2 \approx 0$ made in Eq. (5.17) is reasonable. As shown previously in Fig. 5.1, the regions are large and many pixels are sampled.

5.4 Fixed Pattern Noise

FPN is consistent from image to image and is due to multiple causes including different responsivity of each pixel in the array, differences in clock drive voltages, and dust particles on the detector. FPN is usually removed from the images before processing the data by subtracting two subsequent images. This is done to extend the shot noise limited region so that the gain K can be calculated over the entire dynamic range of the system. It is helpful, however, to calculate and plot the FPN to extract more information from the data. To calculate the FPN, the photon variance (σ_P^2) and read noise (σ_R^2) are subtracted from the total noise as follows:

$$FPN = \sqrt{\sigma_{Total}^2 - \sigma_P^2 - \sigma_R^2}. \tag{5.27}$$

This can then be plotted and compared to the ideal FPN slope of 1, as is seen in Fig. 5.8. Any nonidealities in the FPN curve are helpful in distinguishing different types of nonlinearities in the system.

5.5 Gain Nonlinearity

Gain nonlinearity is a measurement of how the camera gain constant changes as a function of signal. Ideally the gain should have no signal dependence. Gain nonlinearity is measured by plotting the gain vs signal and a linear fit to that data. An example is seen

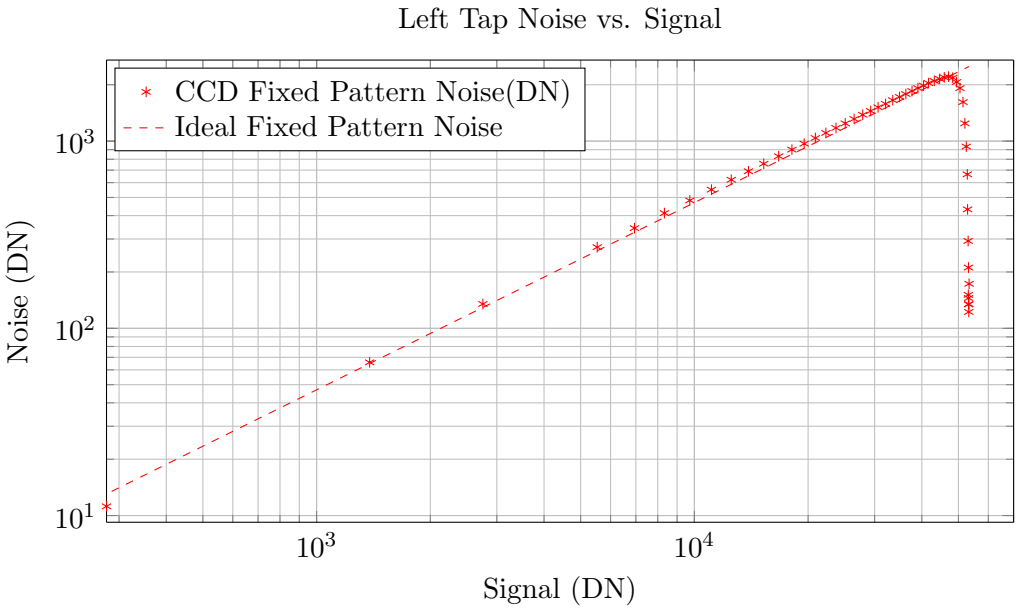

Fig. 5.8: Measured FPN vs. ideal FPN of slope 1.

in Fig. 5.9. The residuals of the linear fit are then taken and the nonlinearity in percent is calculated as follows:

$$\%NL = \frac{\text{rms Error}}{\text{mean Gain}}\text{x}100. \tag{5.28}$$

5.6 Full Well Capacity

FWC is a measure of the number of electrons that each pixel well can hold. This number is found from the saturation point on the PTC. For example in Fig. 4.2 the saturation point is easily seen where the slope suddenly changes.

5.7 Dynamic Range

Dynamic range is calculated as a ratio of the FWC and read noise of the camera system. This also represents the brightest and faintest objects that can be simultaneously discriminated [1, p. 33]. The FWC sets the limit of how bright an object can be and the read noise is the lower limit, where faint objects disappear behind the noise. Thus the dynamic range is the ratio of the FWC to read noise,

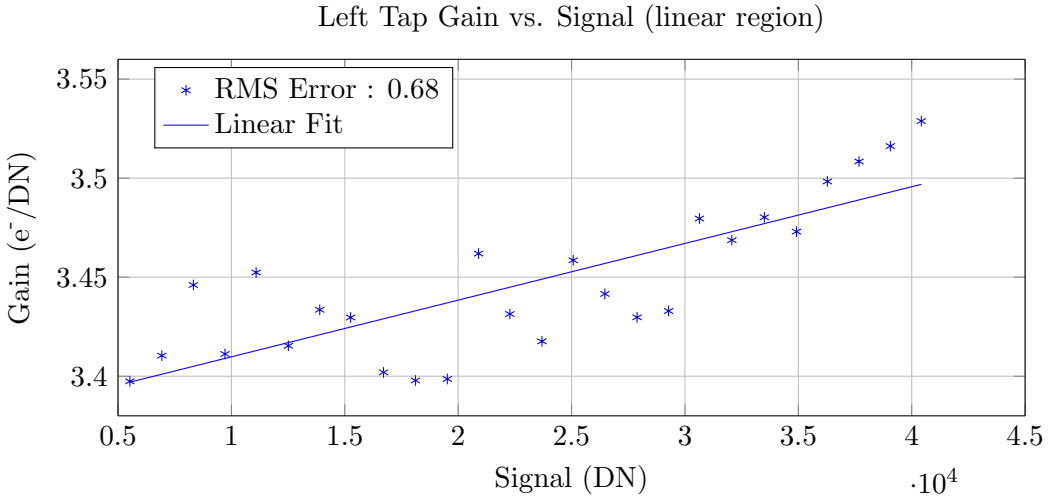

Fig. 5.9: Gain nonlinearity.

$$DR = \frac{FWC}{\sigma_R}. \tag{5.29}$$

5.8 CTE

During charge transfer, some charge gets left behind. The HCTE and VCTE will be calculated from the EPER test. The EPER method is done using a flat field exposure and the overscanned pixels. This method measures CTE by counting the charge that is trapped during transfer. To do this we measure how much charge was left behind in the overscanned pixels. This method is slightly optimistic due to the fact that small amounts of charge left per pixel are hard to distinguish from the noise [9]. This deferred charge is measured in the overscan pixels and then Eq. (5.30) is used to find the efficiency.

$$CTE = (1 - CTI)^{\left(\frac{1}{\#\text{ of Pixel Transfers}}\right)}, \tag{5.30}$$

$$CTI = \frac{\text{Total Deferred Charge}}{\text{Charge Level of Last Active Row}}. \tag{5.31}$$

An example of an HCTE plot where the CTE of each row was calculated is seen in Fig 5.10.

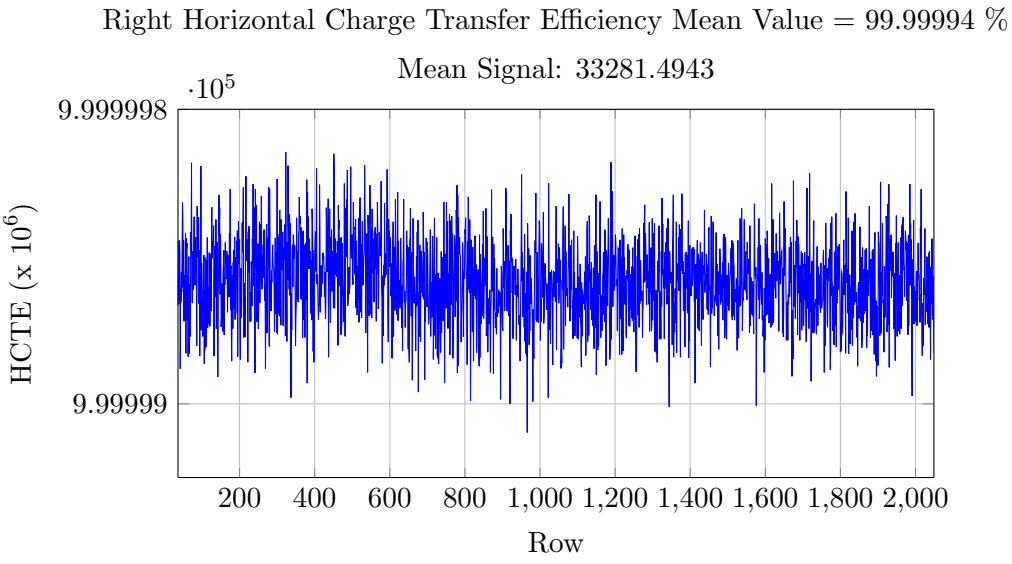

Fig. 5.10: Horizontal charge transfer efficiency.

Chapter 6

Camera System Adjustments

6.1 Faceplate

During characterization it was noticed that the row profiles were brighter on the edges of the CCD. This was unexpected as we were using a uniform source previously verified to $\leq 10\%$ over the image area of interest. An example is shown in Fig. 6.1. Note that the low signal columns in the center are the overscan columns. After discussion, these brighter edges were believed to be due to the faceplate, a metal plate placed around the CCD, causing reflections onto the surface of the CCD as illustrated in Fig. 6.2(a). A proposed change was made (see Fig. 6.2(b)) and after testing, it was verified that the brighter edges were eliminated.

6.2 PTC Adjustments

Other changes were also needed in the camera system to improve performance. To more easily see the linearity of the gain and where improvements were needed, the data was plotted in a Photon Variance Curve (PVC) instead of a PTC. A PVC is just like a PTC

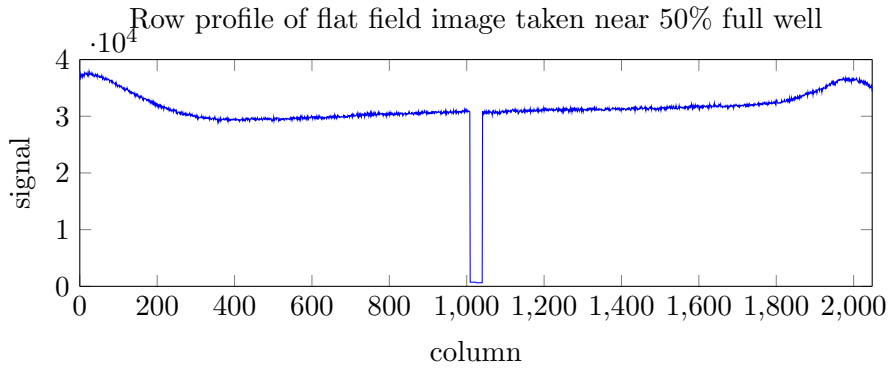

Fig. 6.1: Row profile showing signal peaks near the edge of the image.

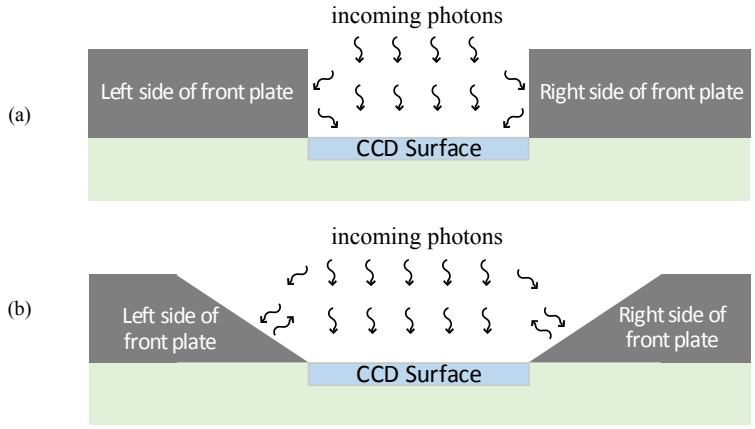

Fig. 6.2: a) previous faceplate model. b) changed faceplate to prevent reflections onto the CCD.

except that variance instead of noise is plotted versus the mean signal response. As seen in Fig. 6.4 the curve did not look like the ideal curve shown previously in Fig. 4.2. It was flattening out before the final saturation point. Janesick explains a similar phenomenon occurring due to an improper voltage bias level [8, p. 72-73]. Noticeable also in Fig. 6.4 is that the signal level continues to increase while the variance curve is flat. Figure 6.3 shows the output schematic of the CCD and the different bias voltages. Through testing it was found that by adjusting the Reset Drain (RD) and Out Drain (OD) bias voltage levels the gain linearity could be improved. These bias levels influence the output node well depth and the output amplifier state.

As seen in Fig. 6.5 when the reset clock is asserted (ϕR) the output node is cleared and set to the voltage level of RD. If RD is not high enough, the well will not be deep enough and can fill up with electrons and overflow back into the summing well (SW). This would cause the pixels to average out, still increasing in signal level, but causing the flattening of the variance curve.

The starting point for the bias voltages was chosen by consulting the data sheet and previous programs that used the same CCD. These voltages were as follows: OD 28.88V, RD 17.24V.

It was next chosen to increase OD to 30V. Doing so resulted in the curve seen in

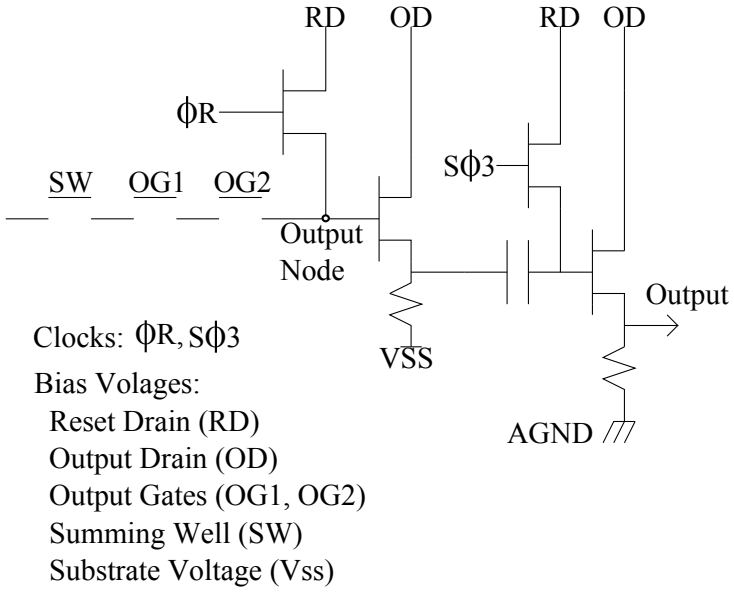

Fig. 6.3: Output schematic of CCD.

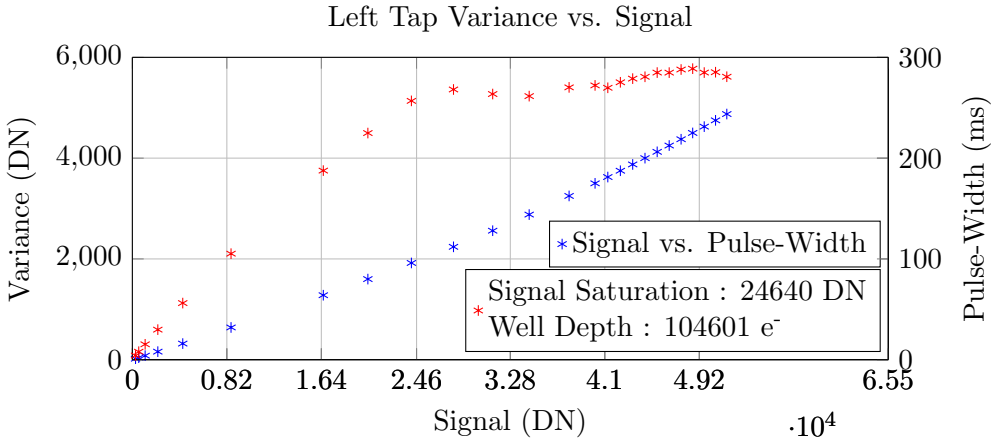

Fig. 6.4: Nonideal PVC showing curve flattening out. OD: 28.88V RD: 17.24V.

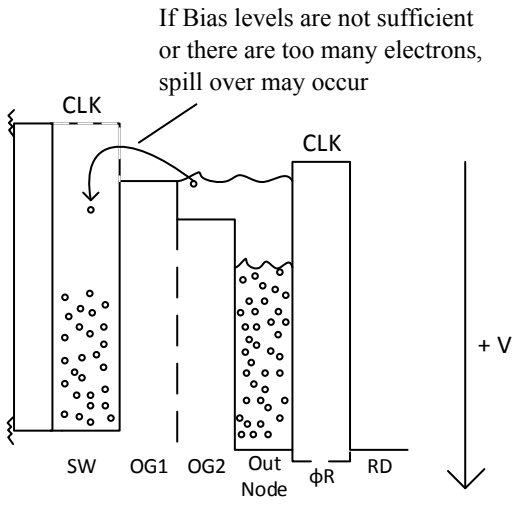

Fig. 6.5: Output of CCD.

Fig. 6.6, where it is no longer flattening out but the saturation curve is not as sharp as is desired. There is also a slight bend in the curve at low signal levels, meaning the low level linearity is poor.

By increasing RD to 17.5V (see Fig. 6.7), the curve begins to flatten out again but the low signal level linearity is improved. It was then chosen to increase RD another volt to 18.5V, leading to the curve seen in Fig. 6.8. The curve now looks nearly ideal with good linearity and a sharp saturation knee curve. In an attempt to increase the well depth, RD was increased to 19.5V. This did increase the well depth, however, the variance curve of the right channel began to flatten out again as shown in Fig. 6.9. RD was next reduced to 19V resulting in the curve seen in Fig. 6.10.

After making adjustments and testing, the bias levels that gave the best results were chosen (RD = 19V, OD = 30V). These are not final flight voltages and may still need to be adjusted after testing is done with the final flight hardware.

The variance after the saturation point in Fig. 6.13, is sporadic. By looking at the images corresponding to these sporadic points, it was found that this CCD displayed a saturation pattern that varied between images. Shown in Fig. 6.11, is the difference of two consecutive images at the same exposure level showing how the pattern differs and can

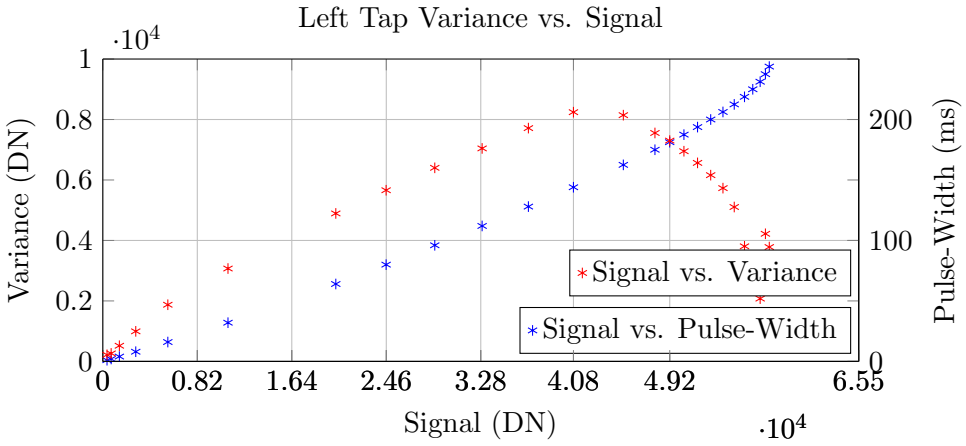

Fig. 6.6: Nonideal PVC showing curve flattening out. OD: 30V RD: 17.24V.

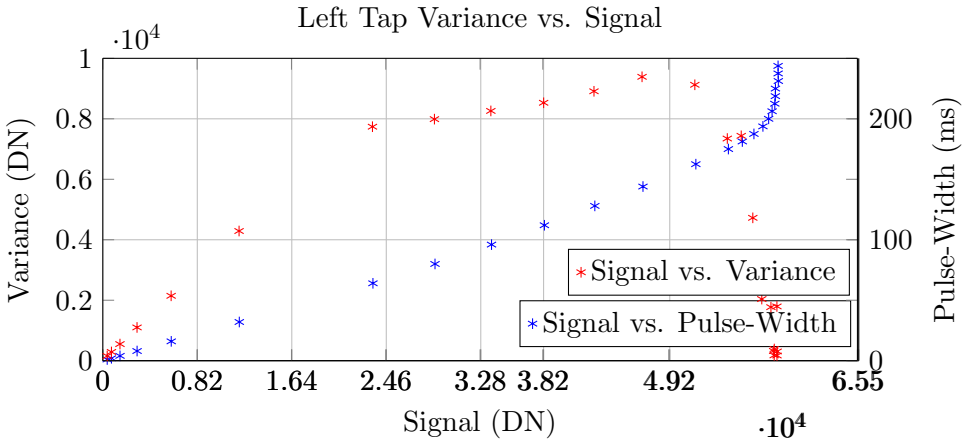

Fig. 6.7: PVC showing improved low level linearity. OD: 30V RD: 17.5V.

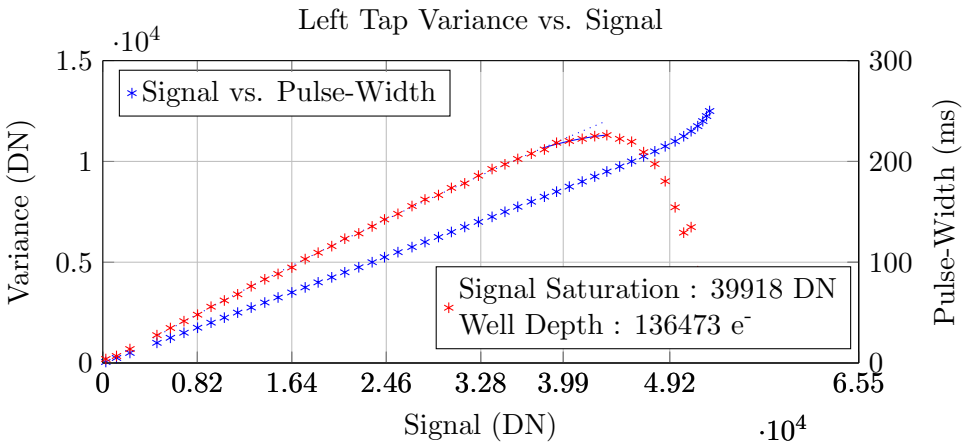

Fig. 6.8: PVC showing nearly ideal characteristics. OD: 30V RD: 18.5V.

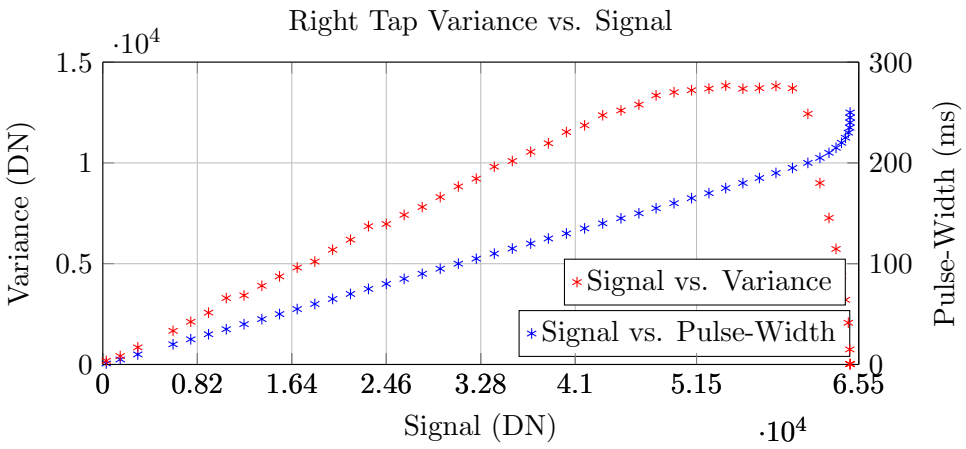

Fig. 6.9: PVC showing increase in well depth but flattening at high signal levels. OD: 30V RD: 19.5V.

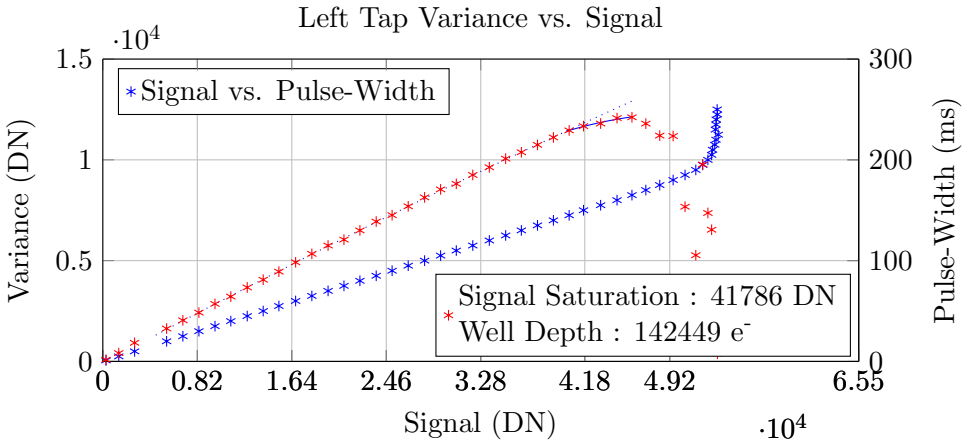

Fig. 6.10: PVC showing larger well depth and nearly ideal characteristics. OD: 30V RD: 19V.

cause this sporadic variance after saturation.

Another nonideality found through the PTC test was that the signal level of the left channel was saturating around 49000 DN in binned mode instead of the desired 65000 DN. The right channel was reaching the desired saturation and both the left and right channels were reaching the desired saturation in unbinned mode. After continuing to test other CCDs it was believed that the early saturation was a characteristic of the left channel of CCD 8-6 as this same behavior was not seen on other CCDs.

6.3 Radiation Tolerance Adjustments

Further adjustments were made due to radiation tolerance requirements. As the CCD is exposed to ionizing radiation, e-h pairs are generated within the gate dielectric and the holes become trapped, generating a flatband voltage that will shift the clock and output amplifier bias potentials [1, p. 722]. If shifted too much the CCD will no longer be in inversion, causing a large increase in dark current. Typical flatband shifts for this e2v device are in the range of 100-200 mV/kRad [10, p. 5]. The expected radiation dose is 2.5kRad over the lifetime of the mission. To include margin the system was designed for a radiation dose of 5kRad. This required the substrate bias voltage to be increased by one volt to 10.5 volts to create an offset for the flatband shift. As the shift occurs due to radiation, the device will still be in inversion. Increasing the substrate bias voltage, however, caused a reduction in FWC as shown in Fig. 6.12. By increasing OD and RD by nearly one volt as well, the decrease in FWC was mitigated.

6.4 CCD Blemishes

There were also some problems found in the engineering model CCDs that could not be fixed or improved such as this column blemish (column that is always bright) shown in Fig. 6.14. This blemish is severe, covering almost the entire height of the CCD and spilling charge into the neighboring columns 828 to 832.

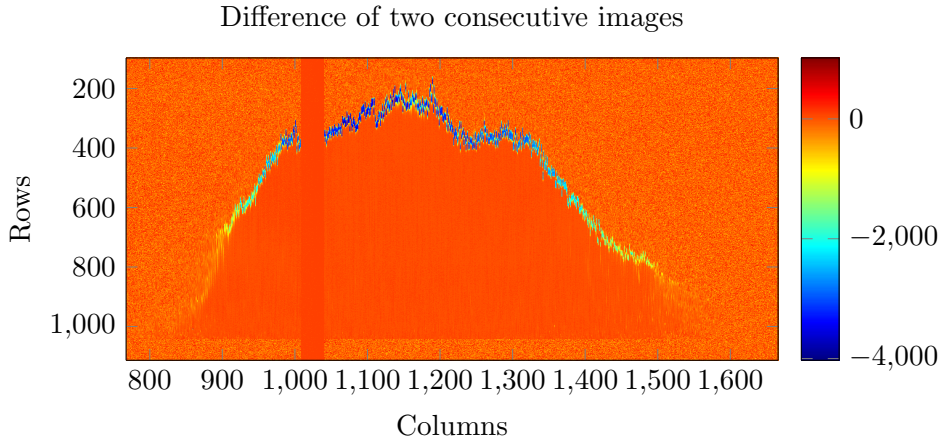

Fig. 6.11: Difference of two consecutive images showing how saturation pattern can cause an increase in variance after saturation.

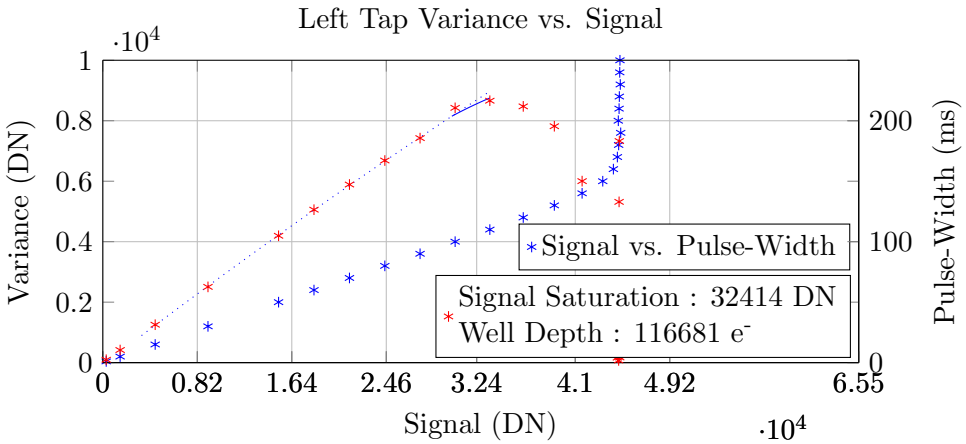

Fig. 6.12: PVC with higher substrate voltage for increased radiation tolerance. OD: 30V RD: 19V SS: 10.5V.

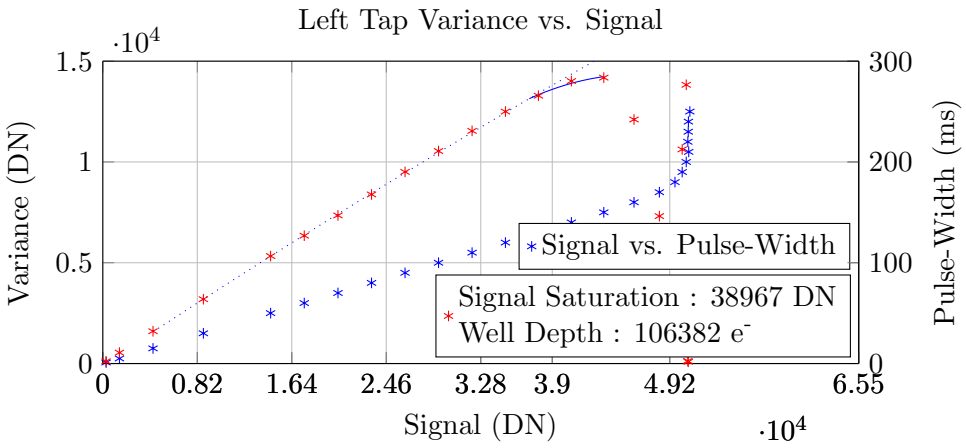

Fig. 6.13: PVC testing if increasing OD further will increase well depth. OD: 31V RD: 19.8V SS: 10.5V.

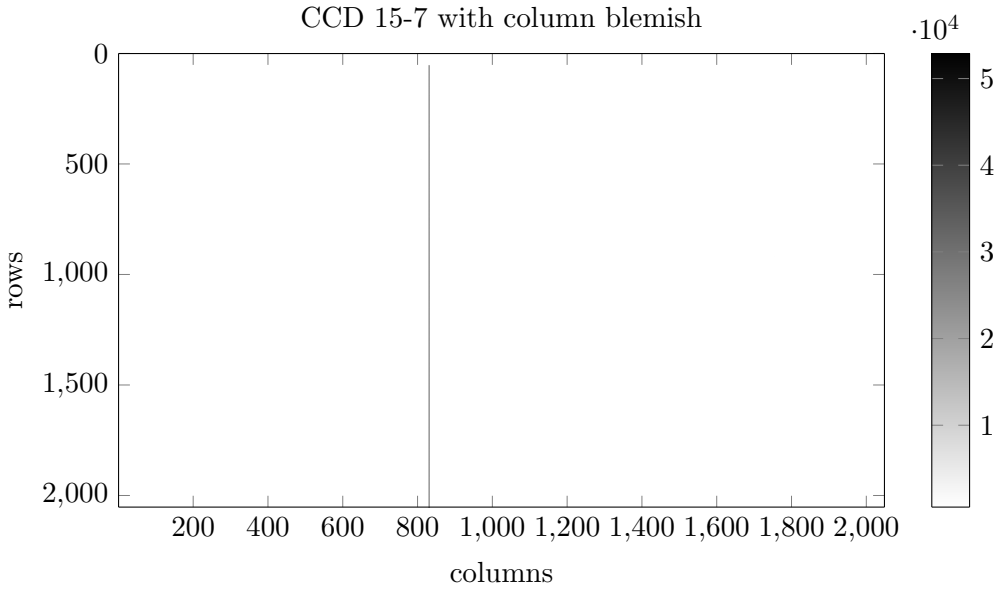

Fig. 6.14: Column blemish in column 830.

6.5 VCTE Adjustments

Although there were no requirements on the VCTE, it is still helpful and interesting to know the efficiencies. In testing there were some difficulties in determining this value. These CCDs from e2v had a bright last column, e2v stated that this was a trait of the CCDs. One possible explanation is that the neutral silicon material outside of the array can generate electrons both thermally and from incident light, which then find their way into the edges of the array ([1, p. 424]). Due to this last bright column, VCTE measurements could not accurately be taken above a signal level near 50% full well. This was because the last row would begin to saturate and bloom (spill over into adjacent rows). This phenomenon is seen in Fig. 6.15. As the last row's charge spills into the following overscan rows, there is more charge in the overscan and thus it seems as though the transfer efficiency is worse. With increasing signal level, the charge is able to spill further and further in both directions. As seen in Fig. 6.16 the charge is beginning to saturate the first overscan row and has bloomed down into row 19 as well.

6.6 Radiation Interference

During data analysis, outlying points were found in the PTCs. These points did not fit into the desired curve. By investigating the image sets corresponding to these points, it was found that bright spots existed in one image and not the next. This behavior was not due to bright pixels or columns as they are consistent between multiple images. As seen in Fig. 6.17 these bright spots caused outlying points in the PTC. Once the two images were subtracted the spot value was much higher (hundreds to several thousand DN) than the average image value (near zero). This increased the mean standard deviation dramatically even though it was only several points out of the entire image area. By filtering these points out, as seen in Fig. 6.17, the PVC becomes more ideal. To filter the spots out, first the two images were differenced pixel by pixel. Then, if the differenced value of any pixel is above a specified threshold, that particular pixel was removed from the calculations. The threshold was set to three orders of magnitude higher than the average difference between images and was adjusted up or down until the outlying points fit the curve well.

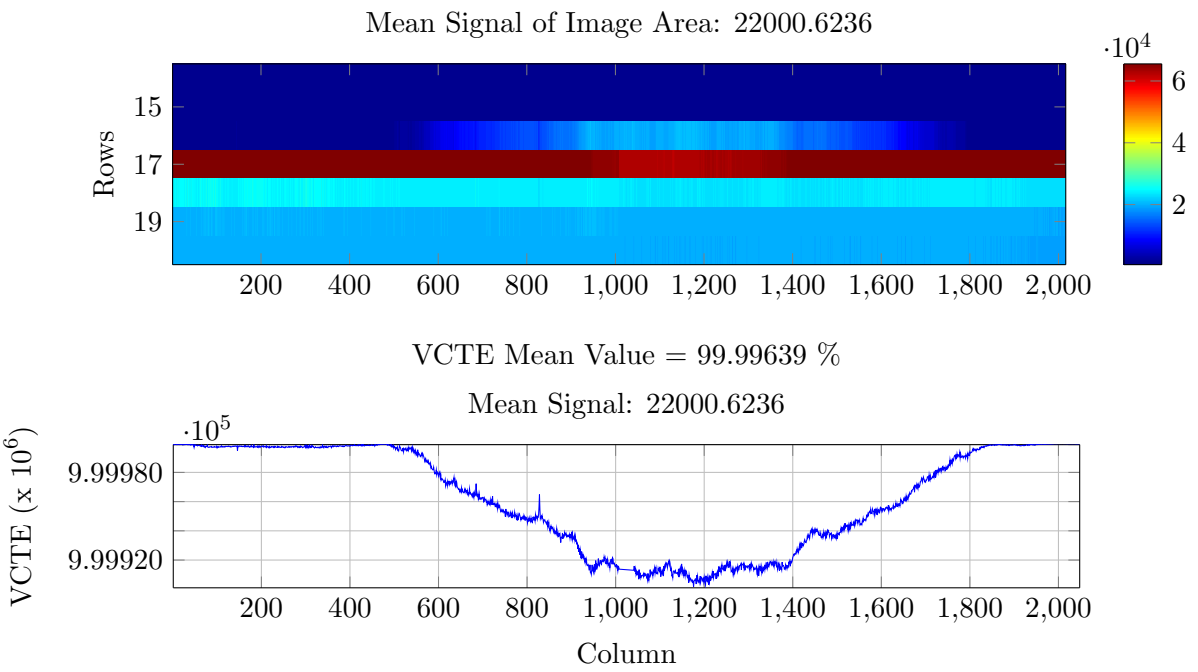

Fig. 6.15: Blooming row showing decrease in VCTE.

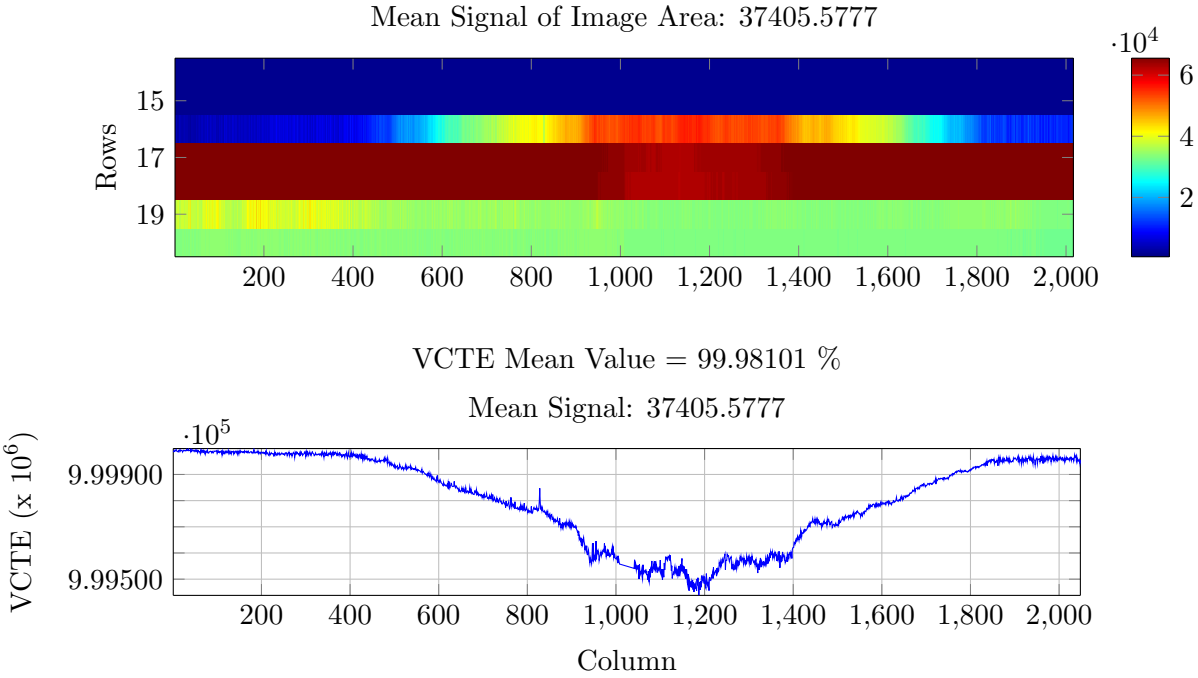

Fig. 6.16: Row continues to bloom in both directions.

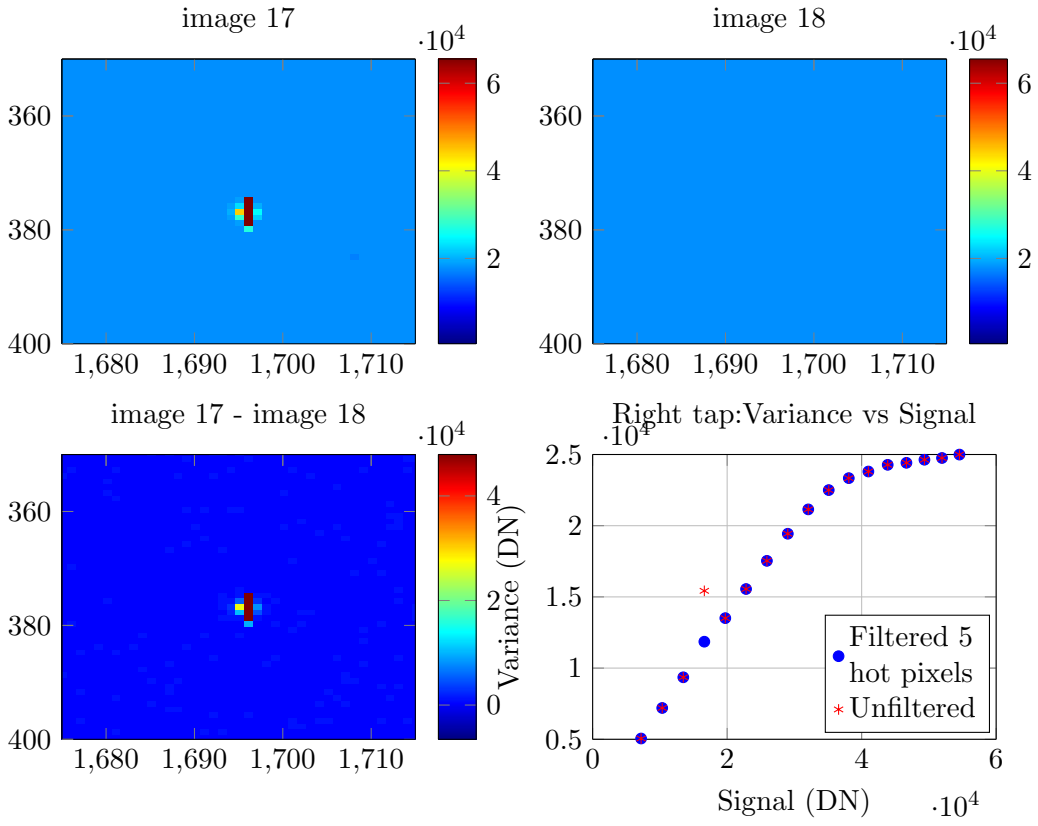

Fig. 6.17: Hot spots creating outliers in PTC.

By investigating these spots, it was found that they are likely due to external radiation. It is not uncommon behavior in CCDs to pick up cosmic rays and other forms of radiation [1]. Figure 6.18 shows an example of some radiation events captured by the CCD. Figure 6.19 shows proton radiation events supplied by Janesick [1, p. 740]. The spots captured by the CCDs are very similar and show the same Bragg peak and tail as those in Janesick's images. Janesick states that the average flux of cosmic rays at sea level is $0.025 cm^{-2} sec^{-1}$ which would equate to about 11 events per min for the area of these CCDs [1, p. 671]. Since Logan, Utah is at a much higher elevation than sea level, approximately 4500ft (1400m) this rate would increase. Other authors have also published papers about detecting radiation interference in CCDs [11].

The amount of energy in the particles can be approximated by calculating how many electrons were generated in its path. However this is not an exact measurement as not all electrons will be distinguishable from noise sources and the particle may have entered and exited the array not releasing all of its energy. The energy of several particles was estimated and found to range from several keV to several MeV which is not uncommon in cosmic radiation.

This is not a complete investigation into the source of these hot spots, however, detecting cosmic rays is a common problem in sensitive CCDs and there is much evidence supporting cosmic rays as the cause. It is only a brief overview of some interesting behaviors found. Further testing would be needed to be sure of the cause.

6.7 Crosstalk

In the process of testing, crosstalk between the output taps was found. Crosstalk, also called ghost images [1, p. 711], are faint images of one output tap showing up or effecting the image of the adjacent tap. As seen in Fig. 6.20, the bright column on the left (output tap-1) causes a darker column on the right (output tap-2). It is a negative ghost image due to the output taps having a shared voltage supply. Figure 6.21 shows the schematics of the CCD output. As charge is dumped to the sense node of output-1 (labeled SN1 in Fig. 6.21), the current through MOSFET-1 is reduced. This, in turn, reduces the voltage

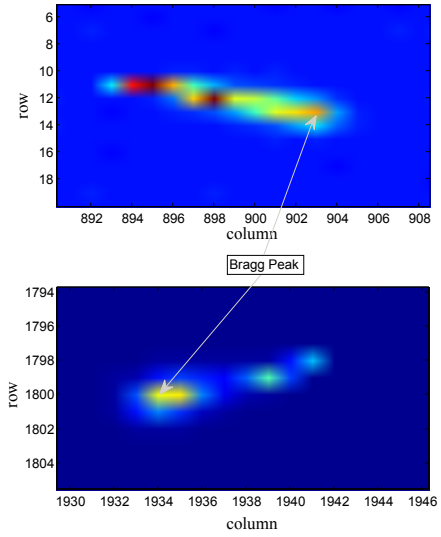

Fig. 6.18: Radiation interference pattern.

drop across the filtering resistor R_{DC}, and increases the voltage supply for output-2 (ΔV_{DD}). This causes an increase in source voltage at the time that video is dumped to the sense node of MOSFET-2. This will subtract from the measured signal causing a negative ghost image [1, p. 712]. This ghost image is very small, only several counts for signals at FWC. However, to reduce the crosstalk, the voltage supply line to the channels will be changed for the flight implementation.

The current layout of the preamp board has the same trace connecting to both output taps. To isolate the outputs from each other in the new layout, the trace is split into separate

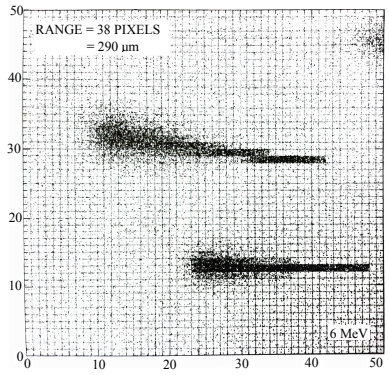

Fig. 6.19: Radiation interference pattern from 6MeV protons.

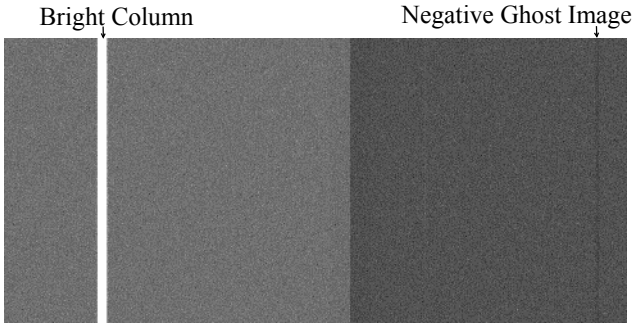

Fig. 6.20: Ghost image seen in right channel due to signal in left channel.

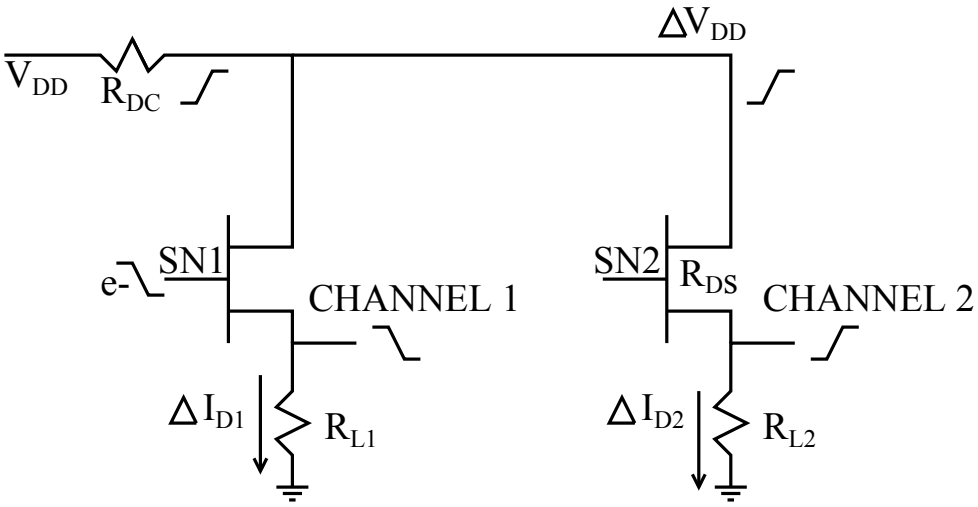

Fig. 6.21: Output schematic of CCD channels showing how ghost images occur.

traces for each output. To further isolate the voltage levels from each other, capacitors have been added at the source and near each output tap's voltage supply pin.

Crosstalk between the two separate camera heads was also found. When each camera head is collecting images, the clocks for one camera interfere with the signal readout of the other camera. This is easily seen in Fig. 6.22. The different effects of the clocking schemes can also be seen. The clocking for charge readout is seen interfering with rows 384 to 1026 and then the fast clocking of the image to storage transfer is seen interfering with rows 207 to 370.

To eliminate the crosstalk, the images can be taken simultaneously by linking the camera commands or by taking the images offset by 15 seconds from each other. Linking the commands causes the clocking of each camera to be synchronized so that no clocks are switching during digitization. Having an offset of 15 seconds would allow the cameras to both be taking images separately yet never overlap readouts. One camera would always be finished reading out before the next one starts, again ensuring that no clocks are switching during digitization.

6.8 Electromagnetic Interference

In the process of testing, noise patterns were found in inverted clock images. These were believed to be due to electromagnetic interference from the surrounding equipment and vacuum pump. Using grounding straps, the camera heads and camera electronics box were grounded to each other and the surrounding equipment. This reduced the noise patterns and read noise levels of 5e- were achieved. When the straps were removed the noise increased to 6e-. There is already a design to have them grounded on the satellite so no further adjustments are needed.

Another source of noise was discovered while testing in a temperature controlled chamber at different temperatures. As is seen in Fig. 6.23, the noise patterns were horizontal bars of varying heights across the image. By analyzing when the noise patterns occurred, and noticing them more often at lower temperatures, it was found that they corresponded to when the liquid nitrogen (LN2) was released into the chamber to reduce the tempera-

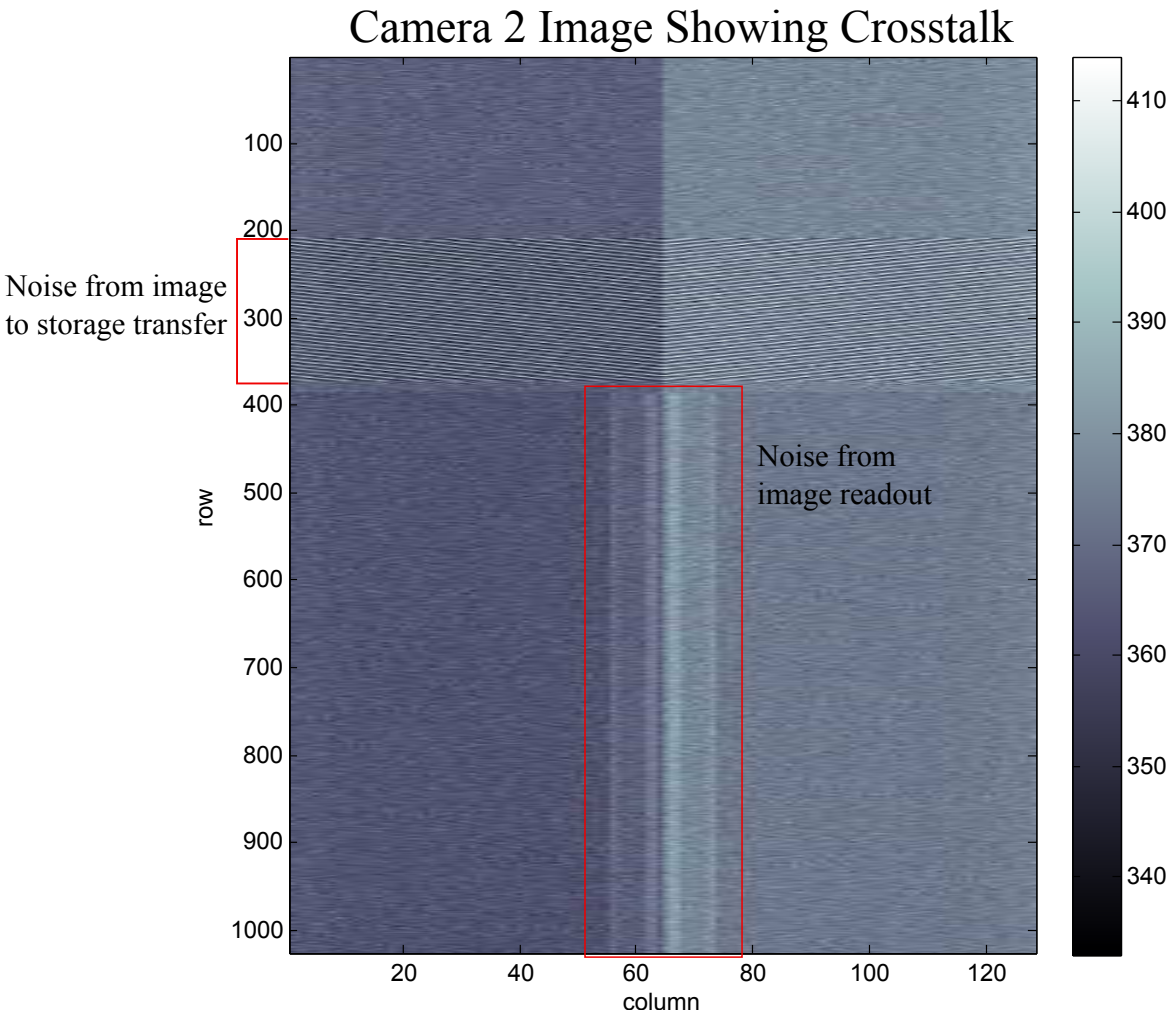

Fig. 6.22: Camera crosstalk.

ture. At lower temperatures this occurred more often. The chamber uses a solenoid valve to release a desired burst of LN2. Longer bursts corresponded with thicker interference bars. No method was found to remove this noise source, except to filter out the corrupted rows of data during analysis.

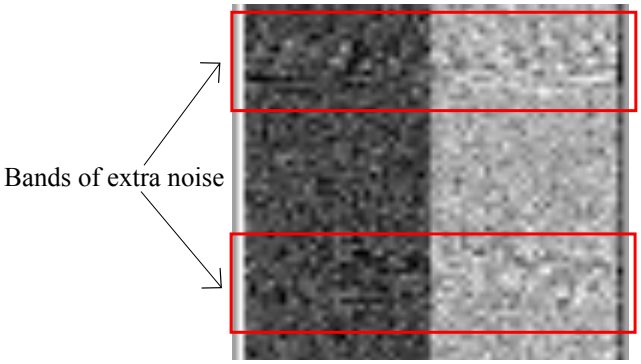

Fig. 6.23: Noise interference due to the LN2 release valve in the temperature controlled chamber.

Chapter 7

Conclusion

During testing some adjustments were made depending on the needs of the engineers and the desired information to be extracted. Such an example was to combine both the HCTE and VCTE tests into the PTC test to speed up the data collections. Through PTC testing, the flattening of the PTC was found to be due to incorrect bias voltages. By adjusting the RD and OD bias voltages, the gain linearity was improved, thus improving the PTC. Several other unanticipated behaviors were found such as the faceplate reflections and radiation interference. The faceplate was changed to fix the problem with the reflections and filtering was included in the data analysis to filter out the radiation interferences. After tuning the camera system, a final data collection and analysis was performed to study the performance metrics of the camera and verify compliance to requirements. Table 7.1 lists the final performance metrics for the different CCDs tested.

CCD 15-7 and CCD 14-7 showed the best results. CCD 15-7 has a column blemish in the Left tap as was shown in Fig. 6.14. CCD 14-7 had very similar results to those of CCD 15-7 and had no column blemishes, because of this, CCD 14-7 was chosen as the Engineering Model (EM) device to send on to the Naval Research Laboratory (NRL) for further testing. The final electronics assembly and CCD 14-7 were found to meet the requirements as outlined in Chapter 2 and Appendix A. As is seen from the results in Table 7.1, the camera system with CCD 14-7 was able to reach a read noise of ≤ 6 electrons and nonlinearity of $\leq 1\%$. The dark current at $-45°C$ was low as well, less than 0.01 electrons per pixel per second. With this performance the instrument is able to collect high quality images used to accurately measure ionospheric wind speeds and directions.

Table 7.1: Final performance characterization metrics.

Performance Metric	**Units**	**CCD 15-7**	**CCD 14-7**	**CCD 8-6***	**CCD 3-8***	**Requirements**
Left Tap Read Noise	e-	5.40	5.66	4.18	80.31	≤ 10
Right Tap Read Noise	e-	5.39	5.74	6.80	80.04	≤ 10
Left Tap Dark Current at 0C	e-/pixel/sec	4.90	9.06	5.07	71.00	—
Right Tap Dark Current at 0C	e-/pixel/sec	4.76	8.96	6.57	68.00	—
Left Tap Dark Current at -45C	e-/pixel/sec	0.0041	0.0075	0.0042	0.0584	≤ 0.13
Right Tap Dark Current at -45C	e-/pixel/sec	0.0039	0.0074	0.0054	0.0566	≤ 0.13
Left Tap Gain	e-/DN	1.35	1.66	1.14	2.90	—
Right Tap Gain	e-/DN	1.35	1.72	1.99	3.24	—
Left Tap Gain Nonlinearity	%	1.13	0.951	7.81	—	≤ 1
Right Tap Gain Nonlinearity	%	0.81	0.999	6.09	—	≤ 1
Left Tap Dynamic Range		12421	14292	13539	1124	—
Right Tap Dynamic Range		12146	14495	12796	1235	—
VCTE	%	99.99199	99.99688	99.96515	99.99822	—
Left Tap HCTE	%	99.99984	99.99474	99.99980	99.99984	—
Right Tap HCTE	%	99.99993	99.93943	99.99993	99.99987	—
* CCD 8-6 and CCD 3-8 were removed from testing early on due to bright dark current patterns and column blemishes. Thus their results were taken before some of the adjustments described in Chapter 6 were made and may be incomplete.						

References

[1] J. R. Janesick, *Scientific Charge-Coupled Devices*. Bellingham, WA, USA: SPIE, 2001.

[2] U. N. R. Laboratory. (2013) Nrl's mighti slated for launch on icon mission. [Online]. Available: www.nrl.navy.mil/media/news-releases/2013/nrls-mighti-slated-for-launch-on-icon-mission

[3] C. Berkeley. (2015) Michelson interferometer for global high-resolution thermospheric imaging. [Online]. Available: icon.ssl.berkeley.edu/instruments/mighti/

[4] E. Christoph, "Michelson interferometer for global high-resolution thermospheric imaging (mighti) instrument critical design review-instrument and science validation," Naval Research Laboratory, Tech. Rep., Mar. 2014.

[5] J. Cook, "Camera heads," Photograph, 2015.

[6] M. Watson, "Inside the camera head," Photograph, 2015.

[7] J. Kristian and M. Blouke, "Charge-coupled devices in astronomy," *Scientific American*, pp. 66–72, 1982.

[8] J. R. Janesick, *Photon Transfer: DN* $\rightarrow \lambda$. Bellingham, WA, USA: SPIE, 2007.

[9] A. Waczynski, E. J. Polidan, P. W. Marshall, R. A. Reed, S. D. Johnson, R. J. Hill, G. S. Delo, E. J. Wassell, and E. S. Cheng, "A comparison of charge transfer efficiency measurment techniques on proton damaged n-channel ccds for hubble space telescope wide-field camera 3," *Trans. Nucl. Sci.*, vol. 48, no. 6, pp. 1807–1814, Dec. 2001.

[10] D. Burt, J. Endicott, P. Jerram, P. Pool, D. Morris, A. Hussain, and P. Ezra, "Improving radiation tolerance in e2v ccd sensors," in *SPIE Optics I& Photonics*, Aug. 2009.

[11] D. Groom, "Cosmic rays and other nonsense in astronomical ccd imagers," Lawrence Berkeley National Laboratory, Tech. Rep., Jan. 2002.

Appendices

Appendix A

MIGHTI Level 5 Requirements

A.1 Physical Requirements

1. CCD shall be a frame transfer device with 2048 X 2048, 13.5 micron pixels.
2. The CCD shall have binning capability.
3. (Goal) CCD QE of $\geq$ 95% @630 nm and 558 nm; and $\geq$ 80% at 760 nm.
4. A TEC will be used to cool the CCD to a target operating temperature of -45°C.
5. Heating the CCD by reversing the TEC polarity shall be possible.
6. The camera structure shall be light tight with the exception of the main opening/window used to illuminate the CCD.
7. The camera shall not vignette an incident telecentric beam with an F-number of f/6.0 over the entire image area.
8. The CCD camera must be capable of room temperature operation in a laboratory environment, in TVAC chambers, and in the vacuum of space.

A.2 Camera Read Out Requirements

1. The CCD read noise shall be less than or equal to 10 electrons rms for a binned pixel.
2. Exposure times of 1 second (or less) to 60 seconds (or greater) shall be supported.
3. (Target) CCD dark current: $\leq$ 0.13 electrons/s at -45°C for a 13.5 μm square pixel.
4. Frame transfer time shall be $\leq$ 340 ms.

5. Read out time for binned frame shall be ≥ 3.8 s.

6. The CCD camera shall digitize the video signal with a 16-bit analog to digital converter.

7. ADC output of 2^{16} DN shall correspond to ≥ 100000 electrons in a "super pixel".

8. Residual nonlinearity shall be $\leq 1\%$ rms across the dynamic range after nonlinearity correction.

Appendix B

CCD Data Sheet by e2v Technologies

e2v technologies

CCD42-80 Back Illuminated High Performance CCD Sensor

FEATURES

- 2048 by 4096 Pixel Format
- 13.5 μm Square Pixels
- Image Area 27.6 x 55.3 mm
- Wide Dynamic Range
- Symmetrical Anti-static Gate Protection
- Back Illuminated Format for Enhanced Quantum Efficiency
- 3-side Buttable Close Butting Package
- Gated Anti-blooming Readout Register (Dump Gate and Drain)
- Low Noise Variable Gain Output Amplifier
- Flatness better than 15 μm peak to valley

APPLICATIONS

- Astronomy
- Scientific Imaging

INTRODUCTION

This version of the CCD42 family of CCD sensors has full-frame architecture. Back illumination technology, in combination with an extremely low noise amplifier, makes the device well suited to the most demanding applications, such as astronomy. To further improve sensitivity, the CCD is manufactured without anti-blooming structures in the image area.

The output amplifier is designed to give excellent noise levels at low pixel rates and can match the noise performance of most conventional scientific CCDs at pixel rates as high as 1 MHz.

The readout register has a gate controlled dump-drain to allow fast dumping of unwanted data. The register is designed to accommodate four image pixels of charge and a summing well is provided capable of holding six image pixels. The output amplifier has a feature to enable the responsivity to be reduced, allowing the reading of such large charge packets.

The device is supplied in a package designed to facilitate the construction of large close-butted mosaics and is designed to be used cryogenically. The design of the package will ensure that the device flatness is maintained at the working temperature.

The sensor is shipped in a protective container, but no permanent window is fitted.

TYPICAL PERFORMANCE (at 173 K)

Pixel readout frequency	20 - 3000	kHz
Output amplifier sensitivity	4.5	$\mu V/e^-$
Peak signal	150	ke^-/pixel
Spectral range	200 - 1060	nm
Readout noise (at 20 kHz)	3	e^- rms
QE at 500 nm	90	%
Peak output voltage	675	mV

GENERAL DATA

Format

Image area	27.6 x 55.3	mm
Active pixels (H)	2048	
(V)	4096 + 4	
Pixel size	13.5 x 13.5	μm

Package

Package size	77.25 x 28.168	mm
Number of pins	36	
Window material	N/A	
Inactive edge spacing:		
sides	260 ± 50	μm
top	150 ± 50	μm

e2v technologies (uk) limited, Waterhouse Lane, Chelmsford, Essex CM1 2QU, UK Telephone: +44 (0)1245 493493 Facsimile: +44 (0)1245 492492
e-mail: enquiries@e2v.com Internet: www.e2v.com Holding Company: e2v technologies plc

e2v technologies inc. 4 Westchester Plaza, PO Box 1482, Elmsford, NY10523-1482 USA Telephone: (914) 592-6050 Facsimile: (914) 592-5148
e-mail: enquiries@e2vtechnologies-na.com

A1A-100025 Issue 9, March 2006
411/9572

PERFORMANCE (at 173 K unless stated)

	Min	Typical	Max	
Peak charge storage (see note 1)	100k	150k	-	e^-/pixel
Peak output voltage (unbinned)		675		mV
Dark signal at 153 K (see note 2)		<0.1	4	e^-/pixel/hour
Charge transfer efficiency (see note 3):				
parallel	99.999	99.9999		%
serial	99.999	99.9993		%
Output amplifier sensitivity	3.0	4.5	6.0	$\mu V/e^-$
Readout noise (see note 4)		3	4	rms e^-/pixel
Readout frequency (see note 5)	-	20	3000	kHz
Output node capacity				
OG2 high	-	1000k	-	electrons
OG2 low	-	200k	-	electrons
Serial register capacity	-	600K	-	e^-/pixel

Spectral Response at 173 K (Astronomy broadband devices)

Wavelength (nm)	Spectral Response (QE)		Response Non-uniformity, max (1σ)	
	Typical	Min		
350	50	40	-	%
400	80	70	3	%
500	90	80	-	%
650	80	75	3	%
900	30	25	5	%

ELECTRICAL INTERFACE CHARACTERISTICS

Electrode capacitances (measured at mid-clock level)

	Min	Typical	Max	
I∅/I∅ interphase	-	35	-	nF
R∅/R∅ interphase	-	80	-	pF
I∅/SS	-	60	-	nF
R∅/SS	-	150	-	pF
Output impedance	-	350	-	Ω

NOTES

1. Signal level at which resolution begins to degrade.
2. Dark signal is typically measured at 188 K and V_{ss} = +9 V. The dark signal at other temperatures may be estimated from:

   $$Q_d/Q_{d0} = 122T^3e^{-6400/T}$$

   where Q_{d0} is the dark current at 293 K.
3. Measurements made using charge generated by X-ray photons of known energy.
4. Measured using a dual-slope integrator technique (i.e. correlated double sampling) with a 10 μs integration period with OG2 = OG1 + 1 V.
5. Readout above 3000 kHz can be achieved but performance to the parameters given cannot be guaranteed.

BLEMISH SPECIFICATION

Traps Pixels where charge is temporarily held. Traps are counted if they have a capacity greater than 200 e^- at 173 K.

Slipped columns Are counted if they have an amplitude greater than 200 e^-.

Black spots Are counted when they have a responsivity of less than 80% of the local mean signal.

White spots Are counted when they have a generation rate equivalent to 100 electrons per pixel per hour at 153 K (typically measured at 188 K). The typical temperature dependence of white spot blemishes is the same as that of the average dark signal i.e.:

$$Q_d / Q_{d0} = 122T^3 e^{-6400/T}$$

Column defects A column which contains at least 100 white or black defects.

GRADE	0	1	2
Column defects	2	6	12
Black spots	500	750	1000
Traps >200 e^-	15	30	50
White spots	250	400	600

Grade 5 Devices which are fully functional, with image quality below that of grade 2, and which may not meet all other performance parameters. Not all parameters may be tested.

TYPICAL OUTPUT CIRCUIT NOISE

(Measured using clamp and sample, temperature range 140 - 230 K)

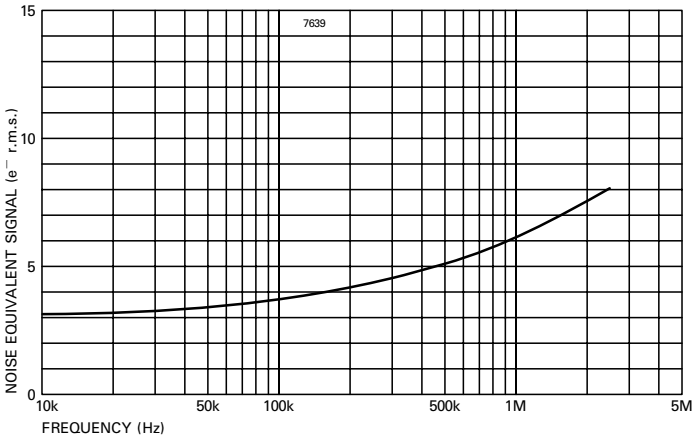

TYPICAL SPECTRAL RESPONSE

(At −90 °C, measured with astronomy broadband AR coating)

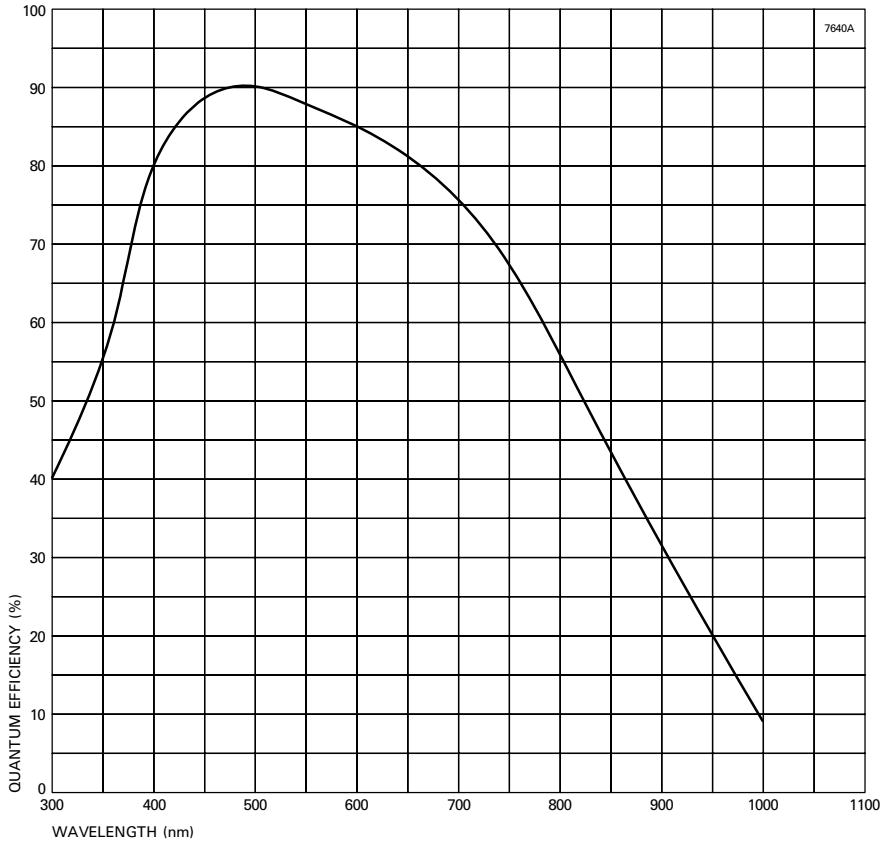

DEVICE SCHEMATIC

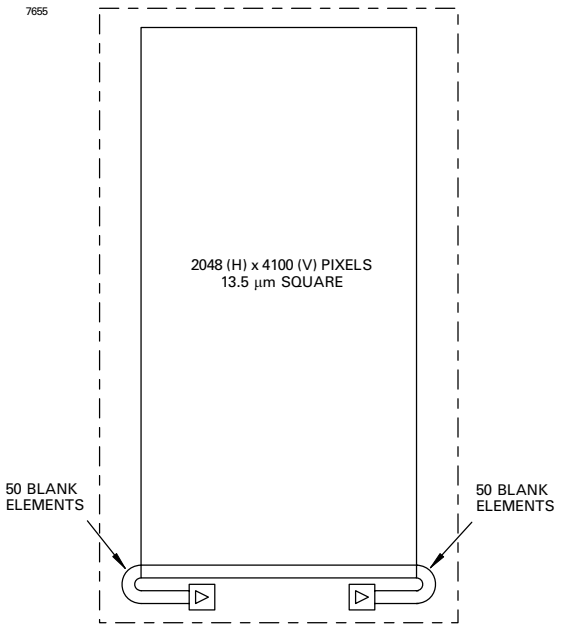

CONNECTIONS, TYPICAL VOLTAGES AND ABSOLUTE MAXIMUM RATINGS

21-pin Micro D-connector

PIN	REF	DESCRIPTION	CLOCK LOW Typical	CLOCK HIGH OR DC LEVEL (V) Min	Typical	Max	MAXIMUM RATINGS with respect to V_{SS}
1	SW(L)	Summing well (left)	0	CLOCK AS RØ3			±20 V
2	DG	Dump gate (see note 6)	0	-	12	15	±20 V
3	ØR(L)	Reset gate (left)	0	9	12	15	±20 V
4	RØ2(L)	Register clock phase 2 (left)	1	9	11	15	±20 V
5	RØ1(L)	Register clock phase 1 (left)	1	9	11	15	±20 V
6	RØ3	Register clock phase 3	1	9	11	15	±20 V
7	RØ1(R)	Register clock phase 1 (right)	1	9	11	15	±20 V
8	RØ2(R)	Register clock phase 2 (right)	1	9	11	15	±20 V
9	ØR(R)	Reset gate (right)	0	9	12	15	±20 V
10	DG	Dump gate (see note 6)	0	-	12	15	±20 V
11	SW(R)	Summing well (right)	0	CLOCK AS RØ3			±20 V
12	OG1(L)	Output gate 1 (left)	n/a	2	3	4	±20 V
13	SS	Substrate	n/a	0	9	10	-
14	IØ2	Image area clock, phase 2	0	8	10	15	±20 V
15	IØ1	Image area clock, phase 1	0	8	10	15	±20 V
16	IØ3	Image area clock, phase 3	0	8	10	15	±20 V
17	-	No connection	-	-	-	-	-
18	-	No connection	-	-	-	-	-
19	-	No connection	-	-	-	-	-
20	SS	Substrate	n/a	0	9	10	-
21	OG1(R)	Output gate 1 (right)	n/a	2	3	4	±20 V

NOTE

6. This gate is normally low. It should be pulsed high for charge dump.

15-pin micro D-connector

PIN	REF	DESCRIPTION	CLOCK LOW Typical	CLOCK HIGH OR DC LEVEL (V) Min	Typical	Max	MAXIMUM RATINGS with respect to V_{SS}
1	DD	Dump drain	n/a	20	24	26	−0.3 to 30 V
2	RD (L)	Reset drain (left)	n/a	15	17	19	−0.3 to 30 V
3	OG2(L)	Output gate 2 (left) (see note 7)	4	16	20	24	±20 V
4	-	No connection	-	-	-	-	-
5	-	No connection	-	-	-	-	-
6	OG2(R)	Output gate 2 (right) (see note 7)	4	16	20	24	±20 V
7	RD(R)	Reset drain (right)	n/a	15	17	19	−0.3 to 25 V
8	DD	Dump drain	n/a	20	24	26	−0.3 to 30 V
9	OD(L)	Output drain (left)	n/a	27	29	31	−0.3 to 35 V
10	OS(L)	Output transistor source (left)	n/a	see note 8			−0.3 to 25 V
11	SS	Substrate	n/a	0	9	10	-
12	SS	Substrate	n/a	0	9	10	-
13	SS	Substrate	n/a	0	9	10	-
14	OS(R)	Output transistor source (right)	n/a	see note 8			−0.3 to 25 V
15	OD(R)	Output drain (right)	n/a	27	29	31	−0.3 to 35 V

If all voltages are set to the typical values operation at, or close to, specification should be obtained. Some adjustment within the minimum - maximum range specified may be required to optimise performance.
Maximum voltage between pairs of pins: OS to OD ±15 V.
Maximum current through any source or drain pin: 10 mA.
The CCD is not electrically connected to the metal package.

NOTES

7. OG2 = OG1 + 1 V for operation of the output mode in high responsivity, low noise mode. For operation at low responsivity high signal OG2 should be set high.
8. Not critical; can be a 3 to 5 mA constant current source, or 5 to 10 kΩ resistor.
9. Readout register clock pulse low levels +1 V; other clock low levels 0 ± 0.5 V.
10. With the R∅ connections shown this device will operate through both outputs simultaneously. In order to operate from the left hand output only R∅1(R) and R∅2(R) should be reversed.

OUTPUT CIRCUIT

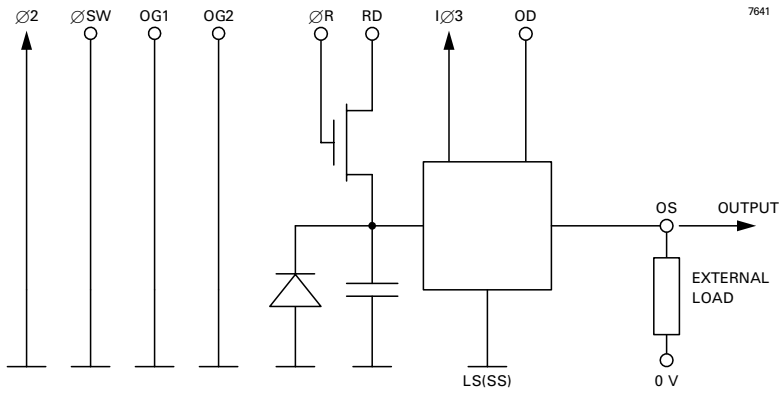

FRAME READOUT TIMING DIAGRAM

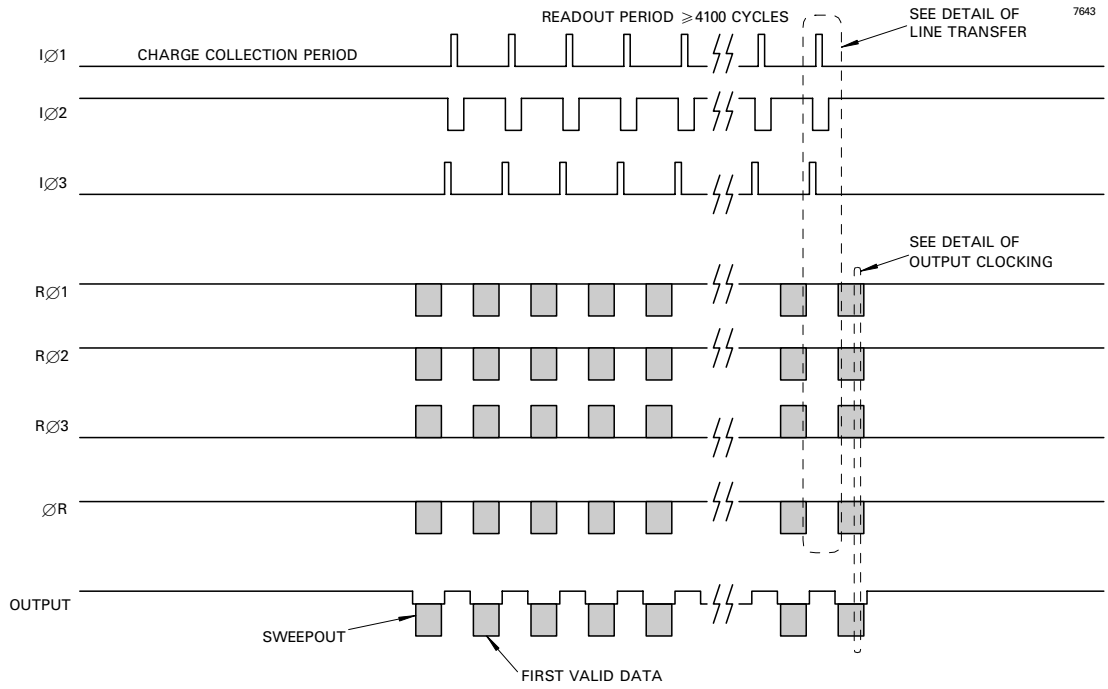

DETAIL OF LINE TRANSFER (Not to scale)

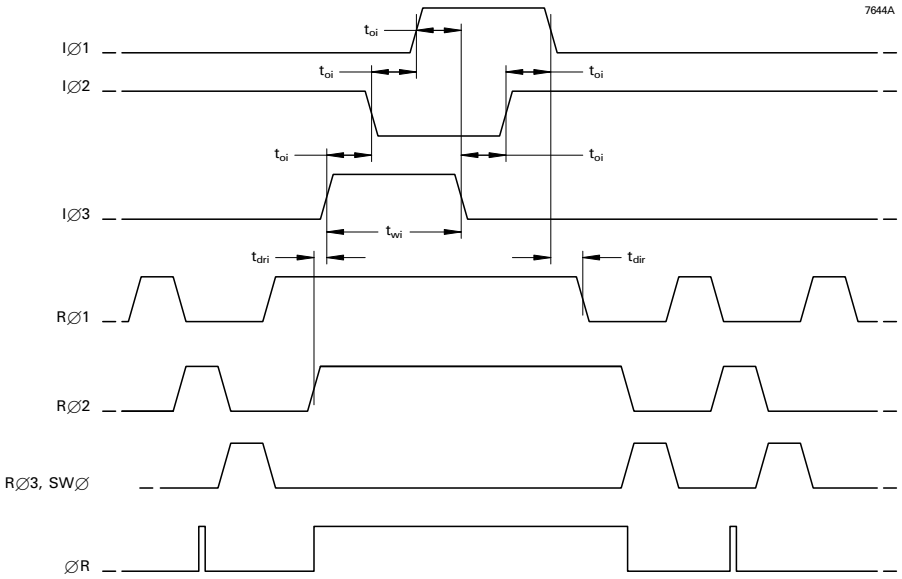

NOTES

11. Clock edges are defined at mid-amplitude points.
12. Rise and fall times should be ⩽ overlap times.
13. Alternate patterns may be used provided sequence and minimum overlaps are maintained.

DETAIL OF VERTICAL LINE TRANSFER (Single line dump)

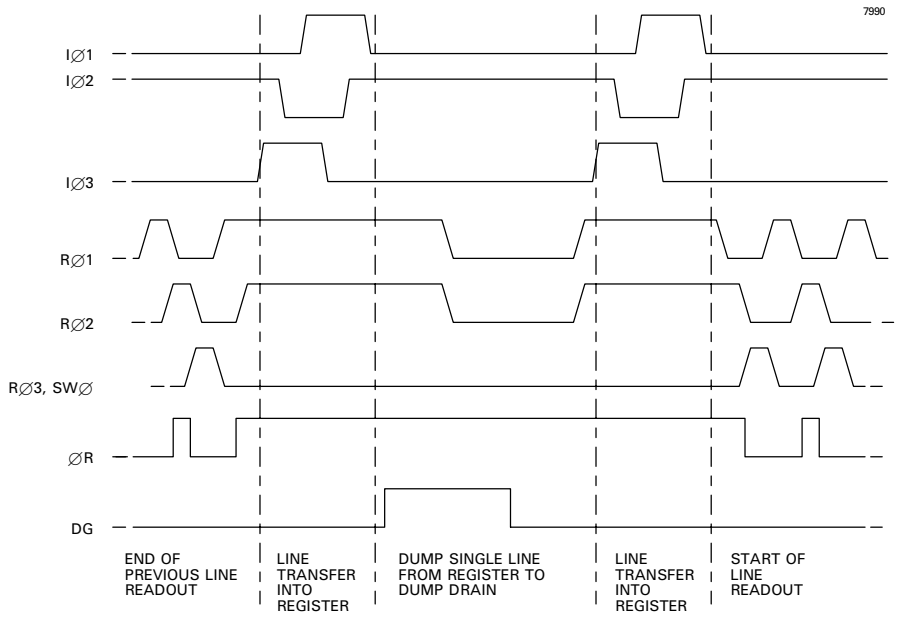

DETAIL OF VERTICAL LINE TRANSFER (Multiple line dump)

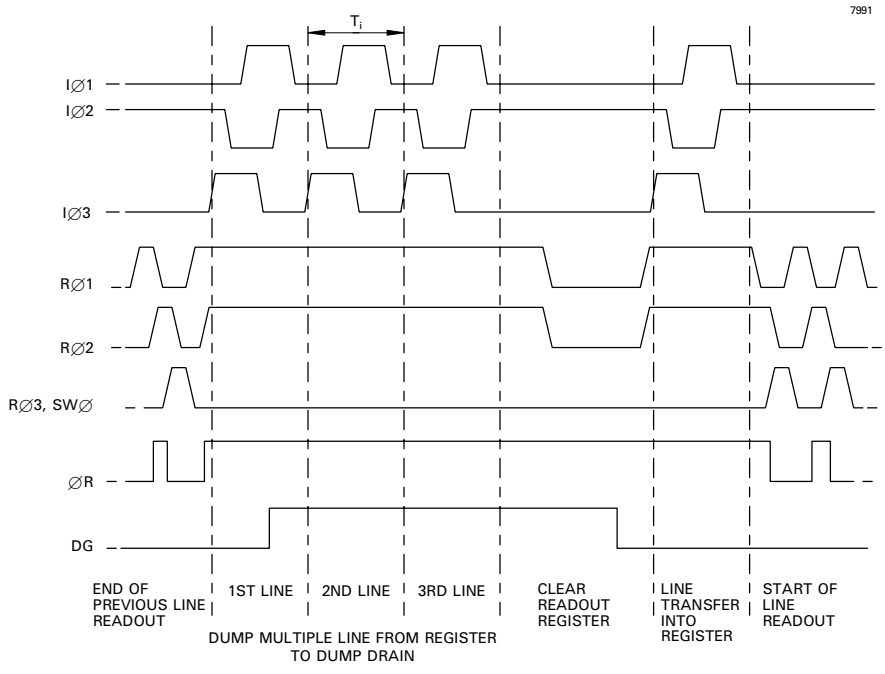

DETAIL OF OUTPUT CLOCKING (Operation through both outputs)

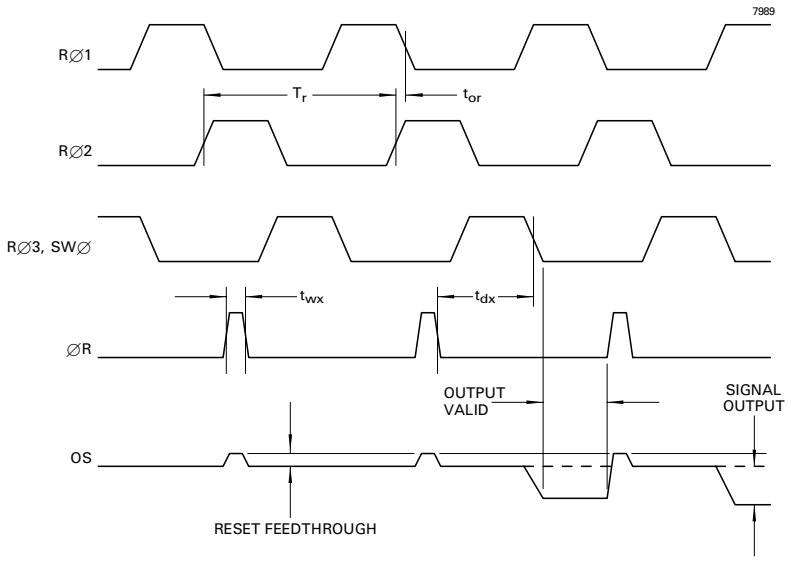

LINE OUTPUT FORMAT (Split read-out operation)

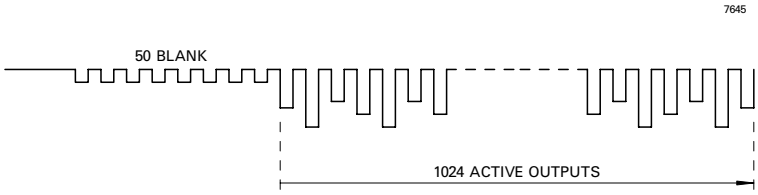

CLOCK TIMING REQUIREMENTS

Symbol	Description	Min	Typical	Max	
T_i	Image clock period	$6t_{oi}$	100	see note 14	µs
t_{wi}	Image clock pulse width	$3t_{oi}$	50	see note 14	µs
t_{ri}	Image clock pulse rise time (10 to 90%)	1	10	$0.5t_{oi}$	µs
t_{fi}	Image clock pulse fall time (10 to 90%)	t_{ri}	10	$0.5t_{oi}$	µs
t_{oi}	Image clock pulse overlap	5	10	$0.2T_i$	µs
t_{dir}	Delay time, IØ stop to RØ start	10	20	see note 14	µs
t_{dri}	Delay time, RØ stop to IØ start	1	2	see note 14	µs
T_r	Output register clock cycle period	300	see note 15	see note 14	ns
t_{rr}	Clock pulse rise time (10 to 90%)	50	$0.1T_r$	$0.3T_r$	ns
t_{fr}	Clock pulse fall time (10 to 90%)	t_{rr}	$0.1T_r$	$0.3T_r$	ns
t_{or}	Clock pulse overlap	50	$0.5t_{rr}$	$0.1T_r$	ns
t_{wx}	Reset pulse width	50	$0.1T_r$	$0.2T_r$	ns
t_{rx}, t_{fx}	Reset pulse rise and fall times	20	$0.5t_{rr}$	$0.2T_r$	ns
t_{dx}	Delay time, ØR low to RØ3 low	50	$0.5T_r$	$0.8T_r$	ns

NOTES

14. No maximum other than that necessary to achieve an acceptable readout time.
15. As set by the readout period (1 µs to 100 µs is typical).

OUTLINE

(All dimensions without limits are nominal)

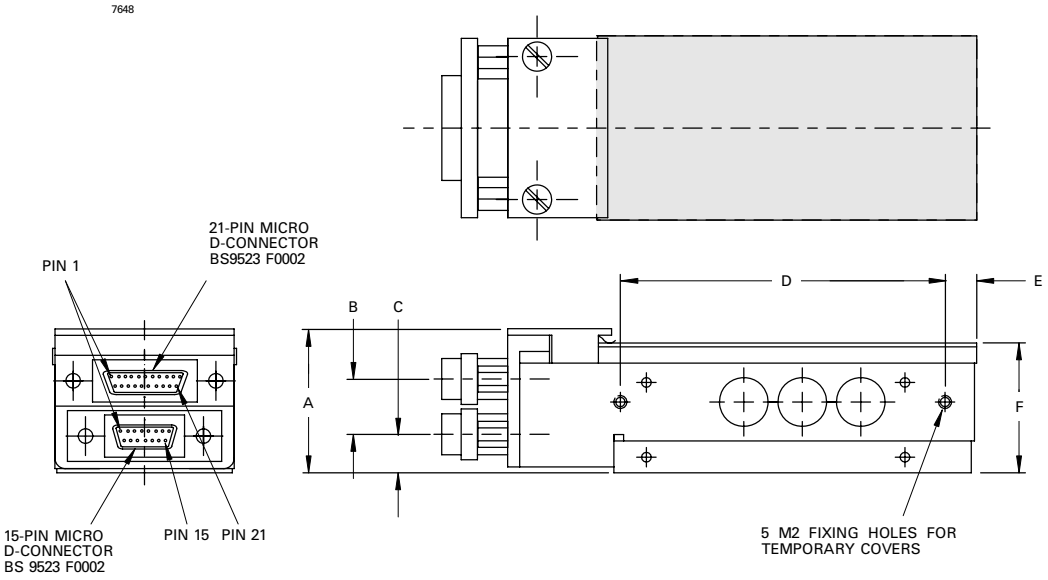

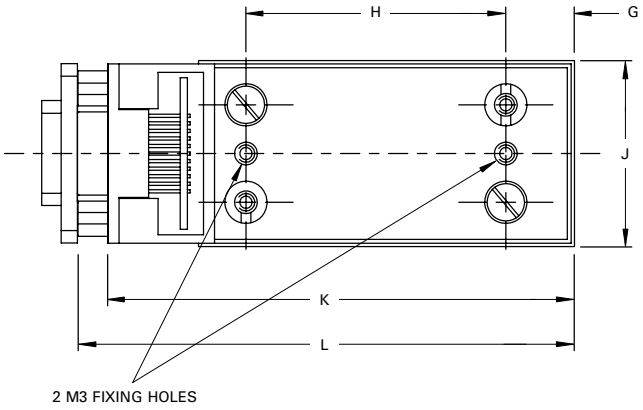

Ref	Millimetres
A	22.50
B	8.50
C	6.00
D	50.00
E	4.83
F	20.00 $\pm$ 0.015
G	10.83
H	40.00
J	28.168 $\pm$ 0.010
K	72.60
L	77.25

HANDLING CCD SENSORS

CCD sensors, in common with most high performance MOS IC devices, are static sensitive. In certain cases a discharge of static electricity may destroy or irreversibly degrade the device. Accordingly, full antistatic handling precautions should be taken whenever using a CCD sensor or module. These include:

- Working at a fully grounded workbench
- Operator wearing a grounded wrist strap
- All receiving socket pins to be positively grounded
- Unattended CCDs should not be left out of their conducting foam or socket.

Evidence of incorrect handling will invalidate the warranty. All devices are provided with internal protection circuits to the gate electrodes (pins 2, 3, 4, 5, 6, 7, 8, 9, 10, 11, 12, 14, 15, 16, 21 on the 21-pin micro D-connector and pins 3 and 6 on the 15-pin micro D-connector) but not to the other pins.

HIGH ENERGY RADIATION

Device characteristics will change when subject to ionising radiation.

Users planning to operate CCDs in high radiation environments are advised to contact e2v technologies.

TEMPERATURE LIMITS

	Min	Typical	Max	
Storage	73	–	373	K
Operating	153	173	323	K

Operation or storage in humid conditions may give rise to ice on the sensor surface on cooling, causing irreversible damage.

Maximum device heating/cooling			5	K/min